Department of Physics and Astronomy

University of Heidelberg

Bachelor thesis

in Physics

submitted by

Marius Wilm Menzel

born in Bad Segeberg (Germany)

2020

Calibration of the MuPix10 Pixel Sensor for the Mu3e Experiment

This Bachelor thesis has been carried out by

Marius Wilm Menzel

at the

Physikalisches Institut in Heidelberg

under the supervision of

Prof. Dr. André Schöning

Abstract

The MuPix pixel sensor series is designed for the Mu3e experiment with the aim of precise particle tracking while keeping a low material budget. The latest version is the MuPix10, which is the first sensor designed to fulfill all technical requirements of the Mu3e detector. The sensor provides a functionality for single-pixel threshold adjustment, which can be used to unify its detection response regarding different characteristics. The procedure of adjusting the threshold of each pixel is referred to as calibration. This thesis reports on the study of three calibration methods for the MuPix10 sensor, namely signal tuning, noise tuning and timing tuning. Signal and noise tuning have been implemented on MuPix10. With the signal tuning aiming for a uniform signal response, a significant reduction of the threshold dispersion from 11 mV to 4.8 mV was achieved. Further, the method of timing tuning, which aims to reduce the spread of signal propagation delay on the sensor, is investigated theoretically. All three methods mentioned above are compared and their possible utilization for Mu3e is discussed.

Zusammenfassung

Die MuPix-Pixelsensoren werden für das Mu3e-Experiment zur präzisen Teilchenspurmessung bei einem gleichzeitig kleinen Materialbudget entwickelt. Die aktuelle Version ist der MuPix10, welcher als erster Sensor per Design alle technischen Voraussetzungen des Mu3e-Detektors erfüllt. Der Sensor verfügt über eine Funktion zur Variation der Schwellenspannung jedes einzelnen Pixels mit dessen Hilfe die Detektorantwort bezüglich verschiedener Charakteristiken vereinheitlicht werden kann. Diese Methode der Schwelleneinstellung wird auch als Kalibration bezeichnet. Die vorliegende Arbeit beschreibt die Untersuchung von drei Kalibrationsmethoden für den MuPix10-Sensor: Signalkalibration, Rauschkalibration und Zeitkalibration. Signal- und Rauschkalibration wurden dabei auf MuPix10 implementiert. Durch die Signalkalibration, welche auf eine einheitliche Signalantwort des Detektors abzielt, konnte eine Verringerung der Schwellendispersion von 11 mV auf 4.8 mV erreicht werden. Zusätzlich wird der Ansatz der Zeitkalibration, der für einer Vereinheitlichung von Signallatenzen verwendet wird, theoretisch behandelt. Die drei Kalibrationsmethoden wurden miteinander verglichen und ihre mögliche Umsetzung für Mu3e diskutiert.

Contents

Part I

Introduction

1 Motivation

The Standard Model of particle physics is a quantum field theory which describes the current understanding of the fundamental constituents of matter in our universe, the elementary particles. Despite its predictive power and its verification in many particle physics experiments, there are still open questions remaining. For example, the Standard Model does not predict the masses of neutrinos and also does not include gravity as a fundamental force. In order to test extensions of the Standard Model, branching ratios of decays are measured with high precision. Here, unknown particles or processes can result in significant deviations from the Standard Model prediction.
In this context, the Mu3e experiment searches for the charged lepton flavor violating muon decay $\mu^+ \to e^+e^-e^+$. In order to identify the signal decay, it is required to measure the trajectory of the decay products with high precision. Since the detector sensitivity highly depends on the reduction of detection material, a tracking system with a low material budget is required. For this purpose, the MuPix pixel sensors are developed. The current version of the sensor, MuPix10, is the first version fulfilling all technical design requirements of the detector. To achieve uniformity of the sensor matrix regarding different characteristic values, the sensor has to be calibrated. Within this thesis, three calibration methods for the sensor matrix are described: signal, noise and timing tuning. The former two methods were for the first time implemented and investigated on the MuPix10 sensor, while the implementation of the latter one is discussed theoretically. In the end, the tuning methods are compared and a possible implementation for the Mu3e detector is shortly discussed.

2 Theoretical background

2.1 The Standard Model of Particle Physics

The Standard Model covers the electroweak interaction as well as quantum chromodynamics and therefore all fundamental forces with exeption of gravitation. It consists of three generations of spin half fermions, four integer spin gauge bosons and the spin zero Higgs boson. The fermions divide into quarks and leptons which come in six flavors each. Additionally, for each fermion there is an antiparticle which carries opposite generalized charges. The particles of the Standard Model together with their mass, charge and spin are presented in Figure 1.

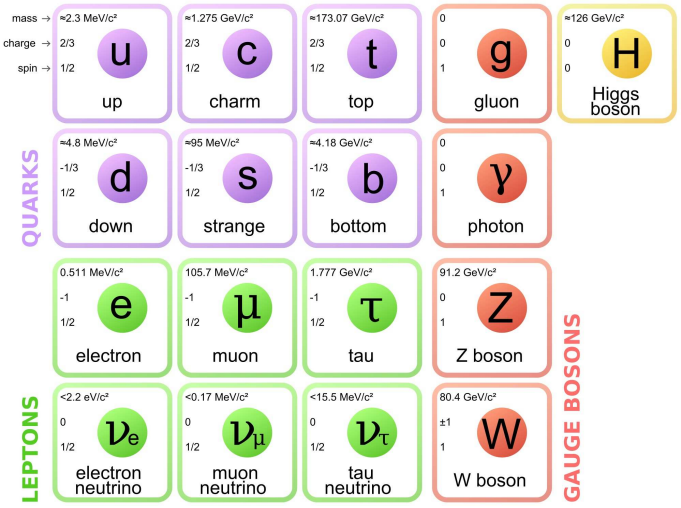

Figure 1: The Standard Model of elementary particles. Taken from [1].

Interactions between fermions are mediated by the bosons, which act as force carriers. For instance, the photon transmits the electromagnetic force while the Z^0 and the $W^{\pm}$ boson are responsible for the weak force interactions. The strong force is mediated by the exchange of gluons. Responsible for the mass of the fundamental fermions and also of the $W^{\pm}$ and Z^0 bosons is the Higgs mechanism with the associated Higgs boson.
The Standard Model integrates the conservation laws of relativity with new conserved quantities, such as the color charge, or the lepton and baryon numbers. The derived conservation laws explain almost all observations made so far by several particle physics experiments.

2.2 Lepton flavor

The lepton number L for a certain state is defined as the amount of leptons minus the amount of anti leptons in that state. It is given by the sum of the the lepton flavor numbers L_e,L_μ and L_τ, which are restricted to leptons of the corresponding flavor. Therefore, the lepton number can be written as shown in Equation 1. Here, N_l refers to the number of leptons belonging to the generation of $l \in \{e, \mu, \tau\}$, while $N_{\bar{l}}$ stands for the number of the corresponding anti leptons.

$$L = L_e + L_\mu + L_\tau = \sum_l N_l - N_{\bar{l}} \tag{1}$$

According to the Standard Model, the lepton number as well as the lepton flavor numbers are conserved in all particle interactions.

2.3 Muon decay

2.3.1 Standard Model decay modes

The leading order contribution to the muon decay is the channel $\mu^- \rightarrow e^- \nu_\mu \bar{\nu}_e$ which is shown in Figure 2. This process is called Michel decay and appears with a branching ratio of nearly 1. The next-to-leading-order process, the inner conversion decay $\mu^- \rightarrow e^- e^+ e^- \nu_\mu \bar{\nu}_e$, however comes with a branching ratio of $BR = (3.4 \pm 0.4) \cdot 10^{-5}$. The to the Michel decay related radiative decay $\mu^- \rightarrow e^- \nu_\mu \bar{\nu}_e \gamma$ occurs with a branching ratio of $BR = (6.0 \pm 0.5) \cdot 10^{-8}$ [2].

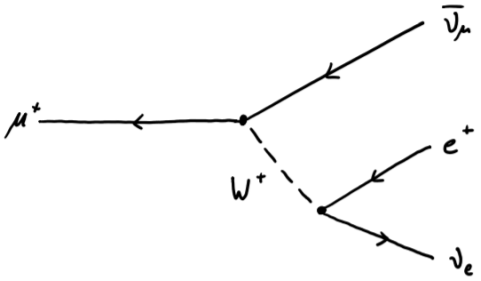

Figure 2: Sketch of the Michel decay.

2.3.2 Decay modes beyond the Standard Model

Considering neutrino oscillations, there is the possibility that a muon decays into three electrons. With it, the change of lepton flavour can be carried out as shown in Figure 3a. However, due to the approximate proportionality of its branching

ratio to $(\Delta m_\nu^2)^2/m_W^4$ and the huge dissimilarity between the W boson mass and the mass difference between the neutrinos, the predicted branching ratio of this decay is $BR = 2.1 \cdot 10^{-55}$ [3]. Therefore, its observation would require such a high sensitivity that it is not experimentally possible to verify in the forseeable future. Nevertheless, some theories beyond the Standard Model predict this decay with a higher BR. For instance, an extension of the Standard Model with an abelian $U(1)$ gauge symmetry introduces a dark photon, which allows this decay. Many other possibilities are as well introduced by the theory of Super Symmetry. An example of such a decay is shown in Figure 3b.

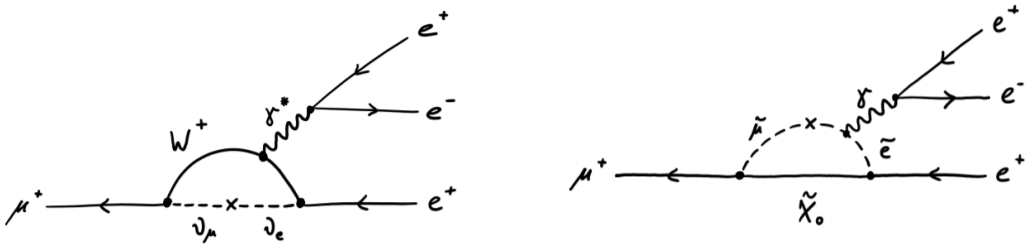

(a) Decay via neutrino oscillation.

(b) Decay via supersymmetric particles.

Figure 3: Muon decay modes beyond the Standard Model.

2.4 The Mu3e experiment

The Mu3e experiment is a fixed-target particle physics experiment which will be carried out at the muon beamline of the Paul Scherrer Institute (PSI) in Villigen, Switzerland. Its main purpose is the search for the charged lepton flavor violating (cLFV) decay $\mu^+ \to e^+e^-e^+$ with a single event sensitivity of $2 \cdot 10^{-15}$ in Phase I. This will be achieved by stopping a high intensity muon beam on a target and observing the decay of the muons. An improvement of the beam intensity is foreseen afterwards, which will increase the sensitivity for Phase II to a value of 10^{-16} [4]. The last experiment dedicated to the search of the $\mu \to eee$ decay was SINDRUM in 1988. Before that, there was a long history of experiments with increasing precision carried out to look for different cLFV decays. An overview of the development of the reached precision is given in Figure 4. The current state of the observations set a limit to the BR of this decay to $< 10^{-12}$ [5].

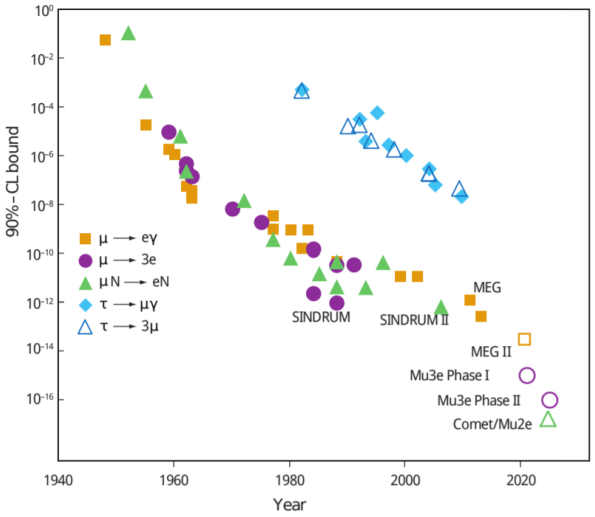

Figure 4: Past and planned experiments searching for lepton flavor violating decays together with their sensitivities. Taken from [6].

2.4.1 Signal and background

The Mu3e experiment is designed to obtain an optimal distinction between signal and background events. Given the nature of the decay, the signal characteristics are well defined. Due to energy and momentum conservation, the decay products i of the $\mu \to eee$ signal decay obey the following kinematic relations in the rest frame of the muon:

$$\vec{p}_{tot} = \sum_{i=1}^{3} \vec{p}_i = 0 \tag{2}$$

$$E_{tot} = \sum_{i=1}^{3} E_i = m_\mu c^2 \tag{3}$$

Therefore, the energy of one decay product cannot exceed half of the resting mass of the muon, which is about $53\,\mathrm{MeV/c^2}$. Furthermore, since the muon decays at rest on the target, all three electrons of the signal decay have to originate from the same point in space-time. Events are considered as background if at least one of those criteria is violated.
In this configuration, two kinds of backgrounds are foreseen: the irreducible and the accidental background, which will be described in the following paragraphs.

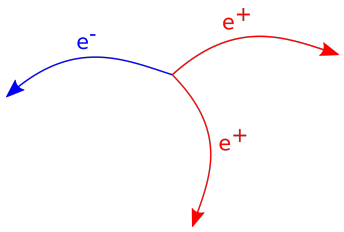

Figure 5: Sketch of the signal decay in the muon rest frame

Irreducible background In Mu3e, the irreducible background is given by the internal conversion decay $\mu^+ \to e^+e^-e^+\bar{\nu}_\mu\nu_e$. Since the involved neutrinos carry away undetected energy and momentum, Equation 2 and 3 are violated for the detected charged tracks. However, for decays with low neutrino momentum, internal conversion decays can imitate a $\mu \to eee$ signal decay due to limits in the detector resolution. In order to suppress this source of background sufficiently, a momentum resolution of less than 1 MeV/c is required [4].

Accidental background Due to the high rates of muon decays within the detector and limited time and spacial resolution, it is possible that electrons of different muon decays appear to be from the same particle. An example of this case is shown in Figure 6a. Here, two positrons from different Michel decays are combined with an electron coming from Bhabha scattering within the detector material, which mimics a $\mu \to eee$ signal decay. Another case of accidental background is when two internal conversion decays occur, but with one produced electron having too little momentum to be detected. This case is depicted in Figure 6b. Both background sources can be reduced with a higher detector resolution.

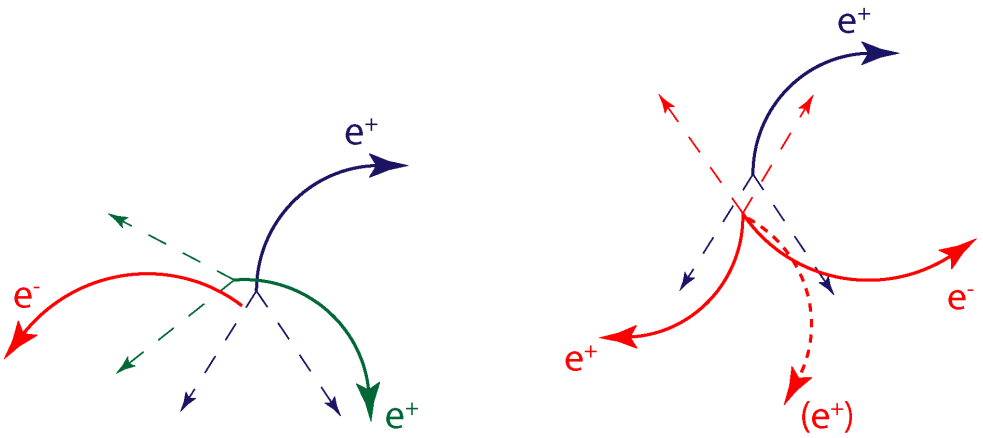

(a) Bhabha scattering.

(b) Internal conversion.

Figure 6: Sketch of accidental background decays.

2.4.2 The Mu3e Detector

The Mu3e detector [7] will be constructed at the Compact Muon Beamline (CMBL) of the Paul Scherrer Institute in Villigen, Switzerland. This is currently the only beamline which fulfills the required antimuon rate of $10^8 \mu^+/s$.
The detector geometry consists of a cylinder coaxial to the beam direction segmented in three barrels along the beam axis. As depicted in Figure 7, the muon beam enters through the first barrel and is then stopped on a hollow double cone target within the central barrel. Afterwards, the emitted decay products pass through the inner pixel layers, which reconstruct the position of the decay vertex with high precision. The inner pixel layers are surrounded by scintillating fibers, which are able to detect the crossing particle with a time precision of a few 100 ps. For this reason, they are used for precise time reference. After the fibers, the decay products pass through the outer pixel layers and recurl due to a magnetic field of around 1 T. From the bending radius of this recurl, the momentum of the particle can be calculated. Finally, the particles pass through the recurl pixel layers an hit scintillating tiles in the outer barrels. The tiles allow to reconstruct the event with a time resolution of around 50 ps.
This setup of the detector allows to achieve a sufficient vertex, momentum, energy and time resolution in order to distinguish between background and signal decays as explained in Section 2.4.1.

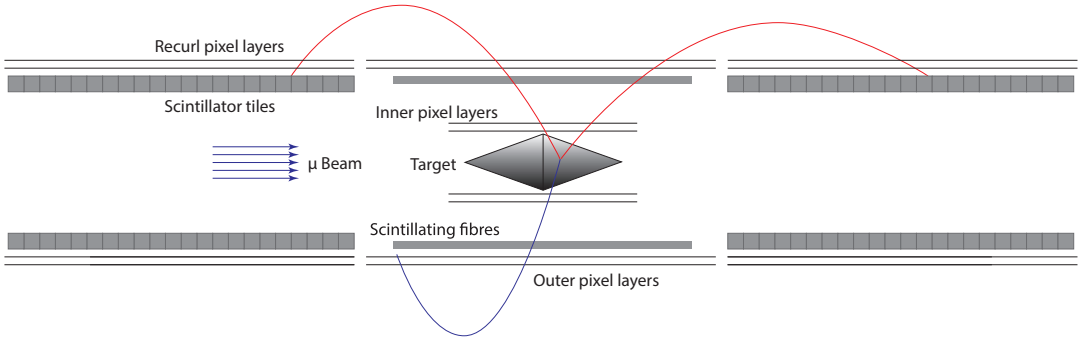

Figure 7: Schematic of the Mu3e detector. Taken from [7].

2.5 Particle interaction with matter

As a free particle traverses through matter it will interact in different ways. Every electrically charged particle can interact via the electromagnetic force, while only hadrons are able to interact via the strong force. Since in Mu3e just electrons

and positrons are detected, the strong interaction is not discussed. Here, the electromagnetic interaction is the dominant process leading to energy loss within the detector material. The energy can be deposited here mainly in four main ways: ionization (or excitation) of its atoms, Bremsstrahlung, Cherenkov radiation and transition radiation. The amount of energy loss in a certain mode depends on the type of particle, its energy and the detector material. Since the energy deposit is a statistical process, it cannot be predicted particle by particle. However, the different processes are well understood, so there are models which describe those statistics with a very high accuracy. In the following sections this will be discussed separately for heavy and light charged particles.

2.5.1 Heavy particles

Particles with a mass higher than the electron are usually referred to as "heavy particles". When these particles cross matter, they mainly loose energy due to ionization. The mean energy loss $\langle \frac{dE}{dx} \rangle$ per travelling length x through material is described by the Bethe-Bloch formula:

$$-\left\langle \frac{dE}{dx} \right\rangle = \frac{4\pi n z^2}{m_e c^2 \beta^2} \left(\frac{e^2}{4\pi\epsilon_0} \right)^2 \left[log\left(\frac{2m_e c^2 \beta^2}{I(1-\beta^2)} \right) - \beta^2 - \frac{\delta(\beta\gamma)}{2} \right] \tag{4}$$

Here, the following parameters and constants are used:

- m_e: rest mass of the electron
- v: velocity of the particle
- c: light velocity in vacuum
- $\beta = \frac{v}{c}$: relative velocity of the particle
- $\delta(\beta\gamma)$: density-effect correction
- n: electron density
- z: charge of the particle in terms of the electron charge
- ϵ_0: vacuum permittivity
- I: mean excitation energy of the material

In Figure 8, the Bethe-Bloch curve is depicted for different materials and particles. Here, all curves show the same general behaviour. Starting from low energy values, the energy loss decreases steeply following a β^{-2} dependency as the particle's energy increases. This happens because the interaction time between the particle

and an atom from the surrounding material increases with lower momenta leading to a higher loss of energy per material length. All of the curves have a global minimum around $\beta\gamma \approx 3$, which is independent of the particle species itself. This means, that for every particle there is a certain momentum range where it looses the least energy. Those particles are called minimum ionizing particles (MIP). With higher momentum, the energy loss increases logarithmically. The reason for this is that the transvers electromagnetical field stretches with higher particle velocity according to the theory of relativity. This leads to a higher interaction strength in transversal direction and therefore to a higher energy loss.

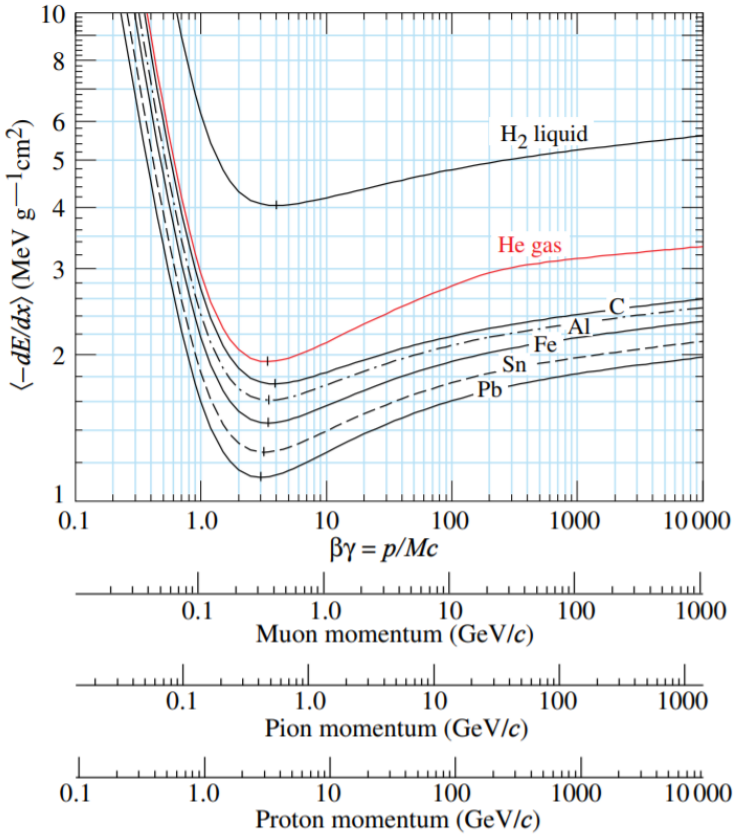

Figure 8: Mean energy loss rate in liquid hydrogen, gaseous helium, carbon, aluminum, iron, tin, and lead for muons, pions and protons. Taken from [2].

2.5.2 Electrons and Positrons

In addition to heavy particles, electrons and positrons show two other effects that contribute to their energy loss. First, Bremsstrahlung plays a significant role for light charged particles, which is not considered in the Bethe-Bloch formula. Second, the incoming electrons can be subject to the Fermi pressure from the material's electrons, while incoming positrons can annihilate with them. Furthermore, incident electrons are indistinguishable from the scattered ones, which does

not apply for positrons. This effect leads to a different energy loss between electrons and positrons. This is considered by the Berger-Seltzer formula for the mean energy loss of electrons and positrons in matter, which is shown in Equation 5.

$$-\left\langle \frac{dE}{dx} \right\rangle = \rho \frac{0.153536}{\beta^2} \frac{Z}{A} \left(B_0(T) - 2log\left(\frac{I}{m_e c^2} \right) - \delta \right) \tag{5}$$

With:

- ρ: material density
- v: velocity of the particle
- c: light velocity in vacuum
- $\beta = \frac{v}{c}$: relative velocity of the particle
- $\frac{Z}{A}$: ratio of protons and nucleons in the material
- $B_0(T)$: momentum dependent stopping power
- I: mean exitation energy of the material
- m_e: rest mass of the electron
- δ: density-effect correction

In Figure 9, the energy loss for each, electrons and positrons, is plotted as a function of their respective momentum. Here, one can see that the general behaviour of both particles is the same, but positrons have a overall higher energy loss due to the effects mentioned before.

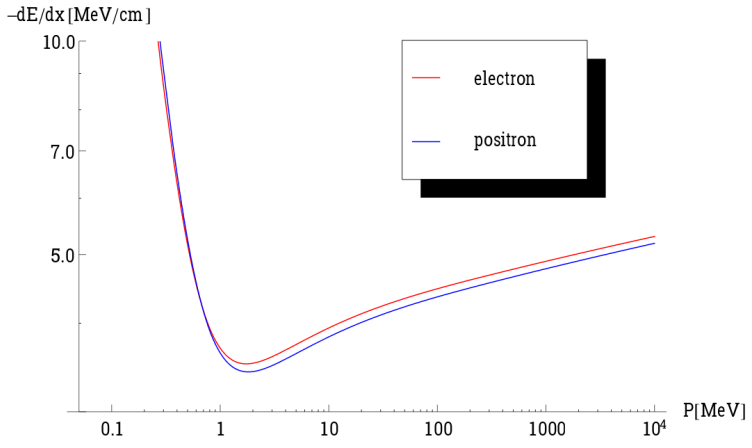

Figure 9: Mean energy loss of electrons and positrons per travelling distance through silicon. Taken from [8] with data from [9].

2.5.3 Multiple Coulomb scattering

As already explained in Section 2.4.1, the background reduction at Mu3e requires high precision particle tracking. However, the passage of a particle through any kind of matter will cause a deflection θ with respect to its initial flight direction. This deflection is a result of many small angle Coulomb scattering processes as shown in Figure 10. For most applications, it is sufficient to describe the angular distribution using a Gaussian approximation. Assuming that the total offset can be neglected in thin material layers, as it is the case for silicon pixel detectors, the root mean square (RMS) of the central 98% of the distribution can be described by the Highland equation:

$$\theta_{rms} = \frac{13.6MeV}{\beta cp} z \sqrt{\frac{x}{X_0}} \left[1 + 0.038 log\left(\frac{x}{X_0} \right) \right] \tag{6}$$

Where z is the fixed charge of the passaging particle, X_0 is the radiation length of the material and x is the travelled distance. In a tracking system, such a deflection alters the particle's momentum and velocity, affecting therefore the tracking resolution. Since the deflection angle depends on the material thickness, this effect introduces tight constraints in the tracking system's material budget.

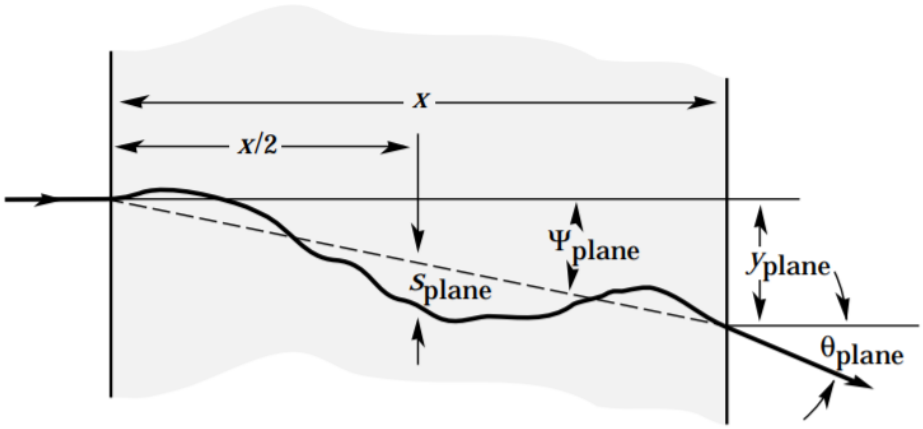

Figure 10: Multiple Coulomb scattering in matter. Taken from [2].

2.6 Semiconductor Physics

2.6.1 Intrinsic Semiconductors

Materials can be in general classified in three categories depending on their conduction properties: conductors, insulators an semiconductors. This distinction depends on the energy gap between valence and conduction band. For conductors, valence and conduction band overlap and there are always free electrons for

charge transportation. For insulators, however, the energy gap is too big and no free electrons are available. Intrinsic semiconductors show unique conduction properties between insulators and conductors. These properties are based on a very small energy gap between the bands. Here, at a temperature of $T = 0K$, all electrons are in a bound state. With higher temperature, electrons are lifted from the valence to a quasi-free state in the conduction band. For every lifted electron, a so called hole is produced in the valence band. Here, the term 'hole' stands for a vacancy in the valence band that acts like a positive charge.

2.6.2 Extrinsic Semiconductors

The conductivity of a semiconductor can be manipulated by a process called doping. This process, in the case of silicon, consists of the insertion of trivalent atoms (acceptors) or pentavalent atoms (donors). If donors are brought into the material, they release free electrons into the conductance band creating an n-doped semiconductor. The same principle applies to acceptors, which create free holes and lead to a p-doped semiconductor. Doping highly affects the charge carrier density of the semiconductor and can be used in order to control its conductivity precisely.

2.6.3 PN-junction

A pn-junction consists of a p-doped semiconductor which is connected side-by-side with a n-doped one. In the junction region, a high electron concentration gradient is formed, as well as a high hole concentration gradient in the opposite direction. This leads to a high diffusion current j_{diff} for both charge carriers, by which electrons from the n-doped region are diffusing into the neutral p-doped region and recombine there with holes. Symmetrically, holes from the p-doped region diffuse towards the n-doped bulk. This leads to a space charge region around the junction as depicted in Figure 11. Within this region, they are nearly no free charge carriers available and therefore it acts as an insulator. For this reason, this region is called depletion zone. The diffusion process forms a charge gradient in the pn-junction region, which then generates a current j_{drift} in the opposite direction. The diffusion is stopped when the two currents have equal strength. At this equilibrium, the diffusion voltage (built-in voltage) V_{bi} is described by:

$$V_{bi} = V_T \, ln\left(\frac{n_A n_D}{n_i^2}\right) \tag{7}$$

with:

$$V_T = \frac{kT}{e} \tag{8}$$

Here, n_A and n_D stand for the concentration of acceptor and donor atoms, while n_i is the intrinsic charge carrier concentration of the semiconductor. The thermal voltage V_T depends on the Boltzmann constant k, the elementary charge e and the

temperature T. The Poisson equation of this system is given through Equation 9, where $\rho(x)$ stands for the charge density function, ϵ and ϵ_0 for the relative and vacuum permittivity, respectively.

$$\frac{d^2V(x)}{dx^2} = -\frac{\rho(x)}{\epsilon_0\epsilon} \tag{9}$$

This equation can be solved in order to find a expression for the total with w of the space charge region:

$$w = \sqrt{\frac{2\epsilon_0\epsilon \cdot V_{bi}}{e}\frac{n_a + n_d}{n_a \cdot n_d}} \tag{10}$$

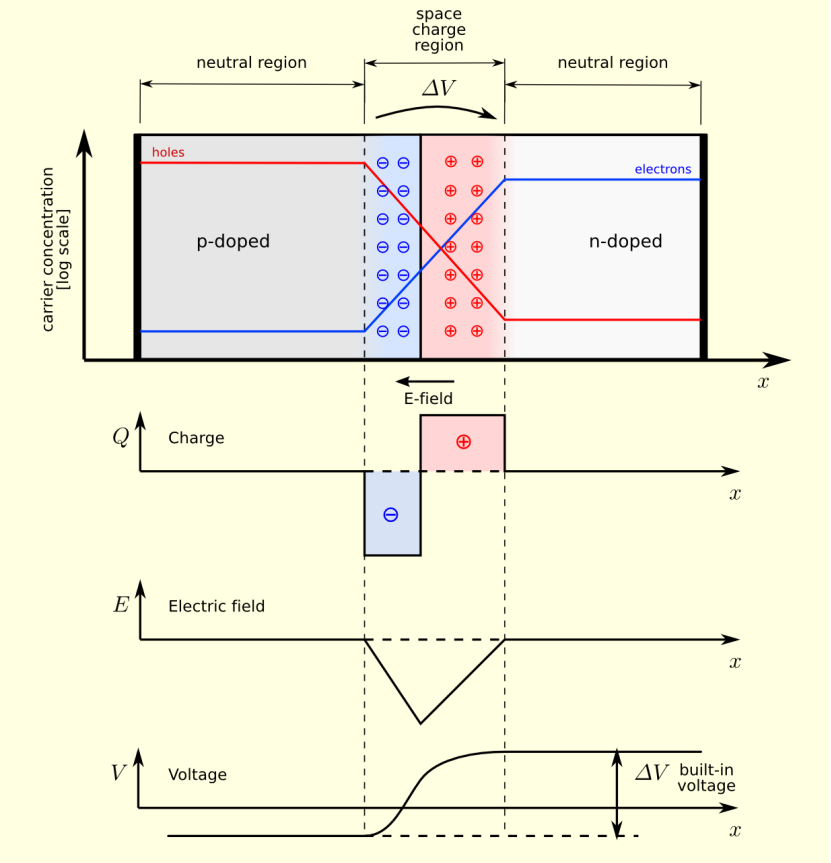

Figure 11: Schematic of a pn-junction diode with qualitative spatial distributions of the charge carrier concentration, the charge Q, the electric field E and the voltage V. Taken from [10].

If the pn-junction is forced out of its thermal equilibrium by an external voltage

V_{ext}, Equation 10 has to be expanded as following:

$$w = \sqrt{\frac{2\epsilon_0\epsilon \cdot (V_{bi} - V_{ext})}{e} \frac{n_a + n_d}{n_a \cdot n_d}} \tag{11}$$

Here, one can see that w decreases in comparison to the static case for $V_{ext} > 0$ since j_{drift} increases. If $V_{ext} \geq V_{bi}$, the space charged region disappears and the diode is fully conducting. In the case that $V_{ext} < 0$, w increases and therefore the insulating region expands. The pn-junction is the base of the semiconductor diode, one of the bottom components of standard electronics. For this reason, it is also referred to simply as diode.

3 Pixel sensors

Pixel sensors are semiconductor detectors which are segmented into independent detection diodes, the so-called pixels. These sensors are commonly used in different applications such as digital cameras or for medical imaging. In high energy physics, pixel sensors are mainly used for particle tracking.

3.1 Semiconductor detectors

As discussed in Section 2.5, a charged particle produces electron-hole pairs when it crosses a bulk of material. In case of a diode, those can be produced either inside or outside the depleted region. In the latter case, the charge carriers diffuse and will eventually recombine. Instead, the charge carriers produced inside the depleted region, are accelerated in opposite direction due to the electric field. The current produced by the moving charges induces a voltage drop at a collection electrode on top of the n-doped zone. The same applies to holes inducing changes to the collection cathode. These voltage drops will then be processed by read-out electronics and used in order to detect the particle.

3.2 Hybrid pixel sensors

Hybrid pixel sensors are commonly used in many high energy particle physics experiments. In general, they consist of two separate entities, one silicon layer used as pixel sensor, and one silicon chip for readout and signal processing. Both layers are segmented in pixels of the same size, and the corresponding pixels of sensor and readout layer are connected via bump-bonds. This technology is for example used in the tracking system of the CMS and ATLAS experiments. A sketch of a hybrid pixel sensor used at CMS is depicted in Figure 12.
The advantages of this technology are multiple. First, the pixel size of these detectors can be very small. Also, given the fact that the active layer can be isolated from the read-out chip, very high reverse bias voltages can be applied. This leads to large depletion regions and therefore large signals with fast charge collection. A disadvantage is the high cost of such a sensor caused by the rather complex fabrication process. Furthermore, the two silicon layers together with the soldering bumps increase the thickness of the whole sensor, which can affect the material budget of a tracking system.

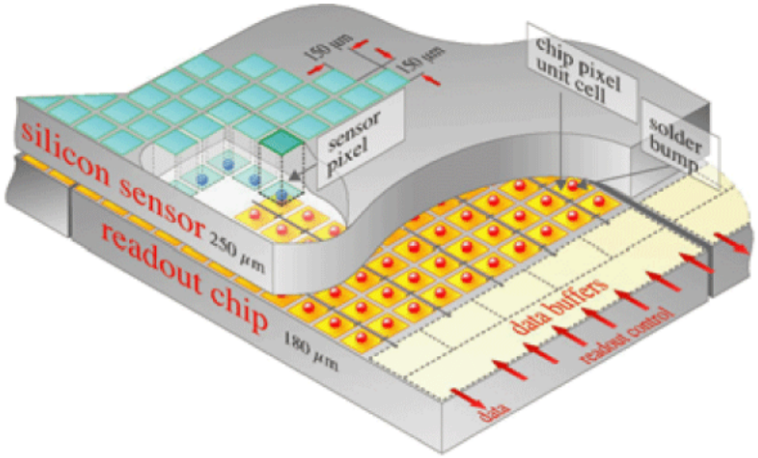

Figure 12: Sketch of a hybrid pixel sensor used in the CMS experiment at CERN. Taken from [11].

3.3 Monolithic Active Pixel Sensors

Monolithic Active Pixel Sensors (MAPS) are based on the technology of active pixel sensors (APS). In the APS pixel design, the read-out electronics is placed in a cell directly next to the active cell inside the active layer. This way, the sensor is fabricated of a single uniform layer. Nonetheless, this design leads to a comparatively small active area of the sensor. However, in the MAPS technology the readout cell is placed on top of the active area. This design leads to complete active sensors. Another advantage is that the CMOS technology used for MAPS is commercial, which decreases production costs and leads also to a higher availability. Furthermore, monolithic sensors can be thinned to thicknesses in the order of 50 μm. However, in conventional MAPS high bias voltages can not be applied. Therefore, the depleted region is only very thin around the pn-junction. For this reason, most of the charge collection happens via diffusion, which has time scales of the order of microseconds, far above the requirements of most high energy physics experiments.

3.4 High-Voltage Monolithic Active Pixel Sensors

In order to achieve the advantages of MAPS together with the fast charge collection via drift, high voltage monolithic active pixel sensors (HV-MAPS) have been developed. A sketch of the concept is shown in Figure 13. Here, n-wells within a p-substrate form the pn-junction. The pixel electronics can be implemented into the n-well (floating logic), which allows a separation from other pixels and from the depletion region. Since the HV-MAPS technology allows to achieve very good

time resolution as well as using little detector material, it was chosen for the Mu3e experiment. The HV-MAPS developed for Mu3e are called MuPix sensors.

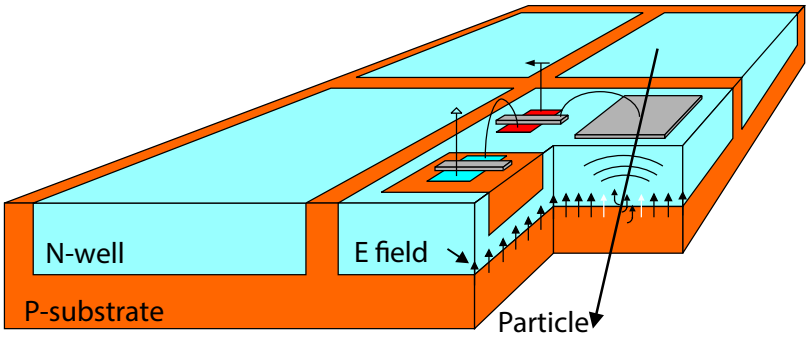

Figure 13: Concept of the HV-MAPS technology. Taken from [7].

Part II

Experimental Setup

4 Setup

4.1 MuPix10 sensor

The MuPix10 [12] is the latest version of the MuPix pixel sensor series. It is the first sensor which is designed to fulfill all required technical specifications of the Mu3e experiment, such as for sensor and pixel size [7]. MuPix10 is implemented in the 180 nm HV-CMOS process of TSI. It has a total size of 20.66 × 23.18 mm and accommodates 256 columns each with 250 pixels. The pixel matrix is divided in three submatrices of 84+86+86 columns. Each submatrix is using its own readout link. A picture of the MuPix10 layout is given in Figure 14.

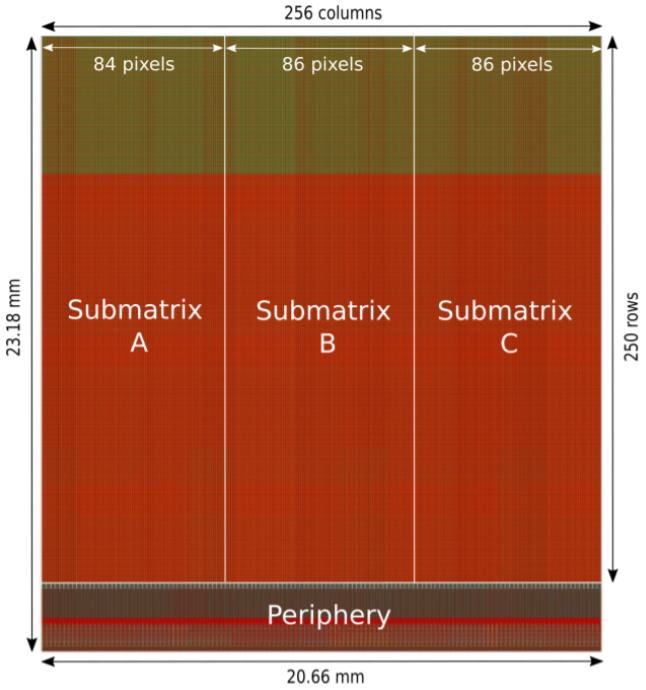

Figure 14: MuPix10 layout.

4.1.1 Chip design

In this chapter, the basic readout concept and the different parts of the MuPix10 sensor will be explained along with the signal flow. Figure 16 provides a simplified overview of the total readout concept.

Pixels MuPix10 consists of 64.000 pixels each with a size of $80 \times 80\,\mu m^2$. The pixel layout can be seen in Figure 15. Whenever a charged particle or a photon hits the active region of a pixel, it creates electron-hole pairs, which induce a mirror charge on the electrodes. The resulting pulse is then amplified by a Charge Sensitive Amplifier (CSA). Another way to induce charge on the capacitor is an external pulse injection. This method will be discussed in Section 4.1.4. After the pulse is amplified by the CSA, it gets directed into the periphery by a line driver.

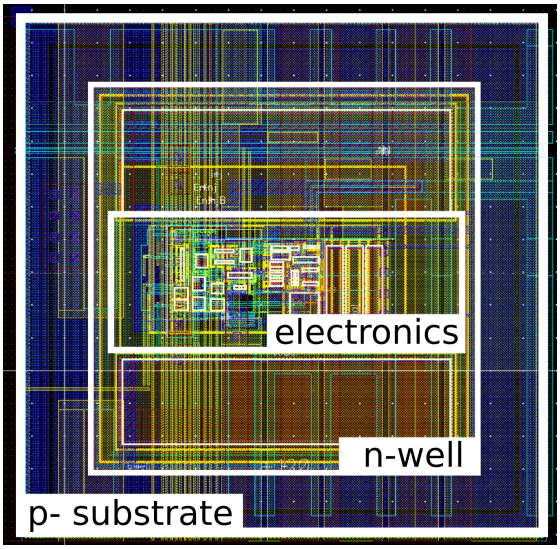

Figure 15: Pixel layout of MuPix10.

Periphery Once delivered to the periphery, the signal is modulated to a constant baseline potential and compared to two threshold voltages (ThHigh and ThLow) by two comparators. If the signal is higher than the threshold value, the corresponding comparator creates a digital output pulse. The length in time of the digital output is equal to the duration the signal height exceeds the threshold voltage. This time duration is a property of the hit and is called "time over threshol" (ToT).

State machine After the digitization of the analog signal, the information from all pixels is gathered in the readout state machine. Here, they are 8b/10b encoded and serialized for further processing.

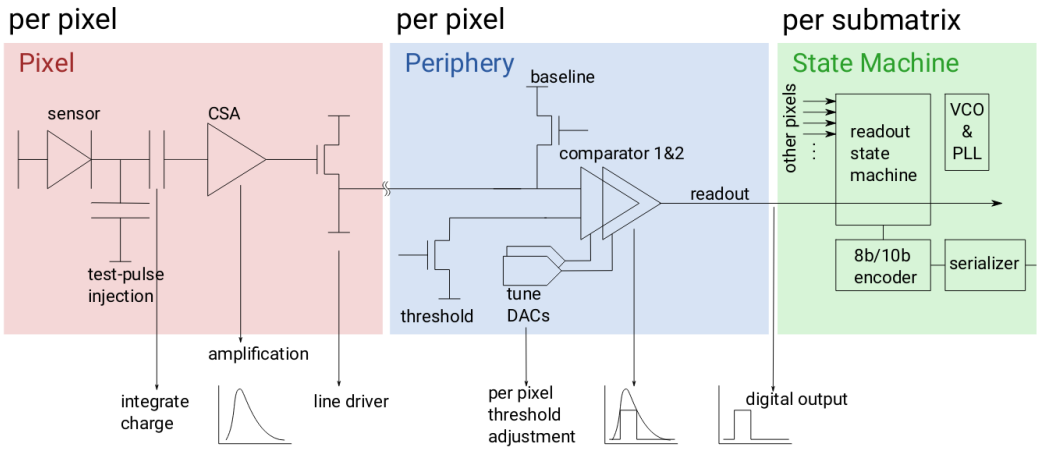

Figure 16: Readout concept of MuPix10. Taken from [13]

4.1.2 DACs

On the MuPix sensors, the value of many electric components, such as active resistances and capacitances, can be controlled by so called Digital to Analog Converters (DACs). From software side, the DACs can be fed with a digital, binary value which directly corresponds to an analog voltage for the addressed electric component. This is an important tool in order to regulate key voltages, optimize components working points and adjust the signal processing of the sensor such that the sensor works suitable for particular tasks. Since the DAC values are discrete, this method of voltage setting gives also a limit on the adjustment granularity.

4.1.3 TDACs

A special kind of DAC on the MuPix10 sensor are the Tuning/Trimming Digital to Analogue Converters (TDACs). Those DACs consist of 7 bits on MuPix10 and are responsible for adjusting the thresholds (ThHigh and ThLow) of the two comparators within the digital cell (see Figure 16). The TDAC can be set for each pixel individually.
As shown in Equation 12, the local pixel threshold Thr_{pixel} is then given through the global threshold Thr_{global} added to the TDAC value multiplied by a tuning factor A. This factor describes the possible tuning strength of the TDACs and is globally given by the DAC value 'VPDAC' which controls the tuning current.

$$Thr_{pixel} = Thr_{global} + A\,(VPDAC) \cdot TDAC \tag{12}$$

The 7 bit TDAC sequence is divided into three parts as shown in Figure 17. The first bit is the so called masking bit. If it is set to 1, the pixel is digitally disabled

for data taking. The three following bits set the threshold value for the first comparator, while the last three bits do the same for the second one.

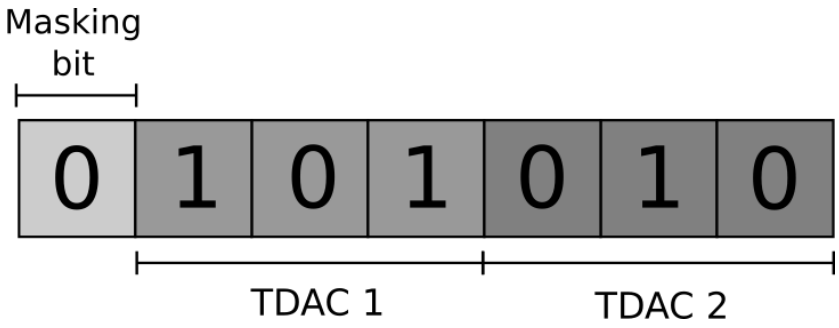

Figure 17: Composition of a TDAC bit sequence.

4.1.4 Injection

As aforementioned, the design of MuPix10 provides an alternative way to receive hit signals instead of real particles, i.e., the injection. This method allows to produce controlled input signals with high frequencies. With this method, artificial hit pulses are generated via the charging and fast discharging of an injection capacitance. This capacitance is connected in parallel to the sensor diode as shown in Figure 18. The fast discharging process imitates the charge deposit of a traversing particle.

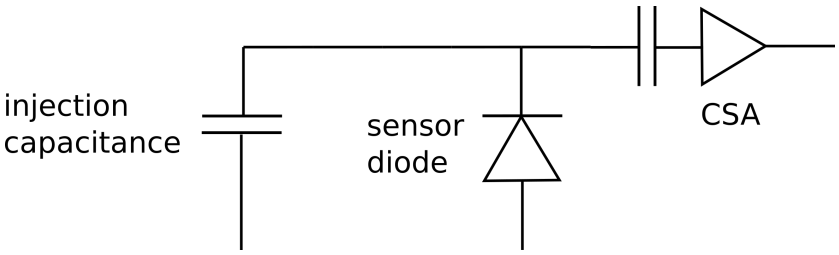

Figure 18: Generation of the injection pulse.

The injection pulses can be adjusted in voltage, duration and frequency. Since the test pulse injection is also designed such that every pixel on the sensor can be addressed individually, the initial injection pulse has to be directed correctly across the sensor. This is done according to the routing scheme shown in Figure 19. Here, the injection voltage is applied from the lower right corner (Column 0, Row 256) of the sensor, from where it is distributed via a connection line across the rows of the sensor. By enabling column transistors, the current can be directed into the chosen column connection, from where the selected pixel can be addressed enabling row transistors.

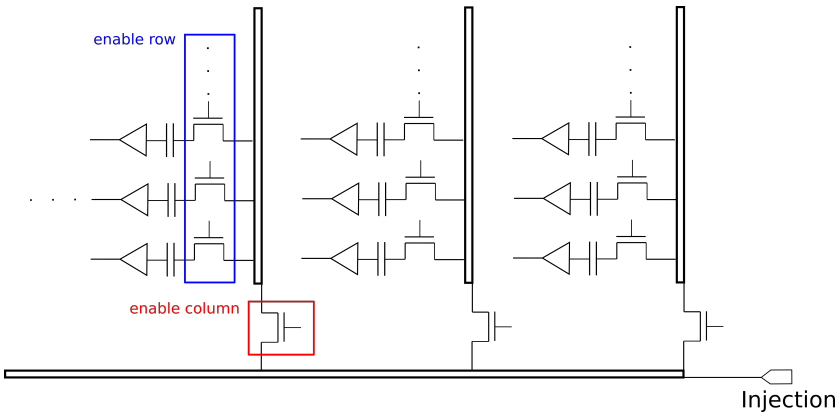

Figure 19: Simplified injection routing scheme of MuPix10.

However, the injection on MuPix10 can only address two pixels at the same time as a smallest unit since one enable row transistor is per design always connected to two pixels of adjacent columns. Within this thesis, this two-pixel-entity is referred to as one double-pixel.

4.2 MuPix10 Insert

The MuPix10 insert is a custom Printed Circuit Board (PCB) which directs the necessary voltages and signals to and from the MuPix10 sensor. It is externally powered using a Molex connector. The sensor connection pads are bonded on the insert via 25 μm thick aluminium wires. The insert also provides different test-points to measure and check applied voltages and test outputs. Figure 20 shows a MuPix10 insert with a bonded sensor.

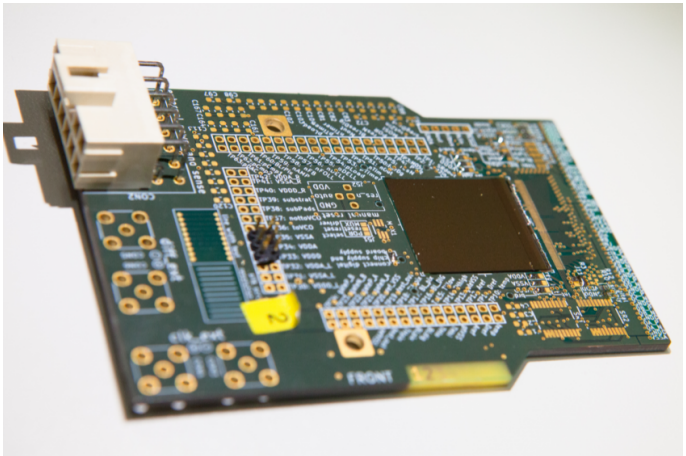

Figure 20: MuPix10 insert with bonded sensor.

4.3 Motherboard

The Motherboard generates and distributes necessary voltages and signals, e.g. for clocks and injection pulses, to the insert PCB. Furthermore, it directs the serialized data from the sensor to the FPGA via a SCSI connector. The supply voltage LVDS of the board, as well as the high voltage are provided by SMA connectors. A picture of the Motherboard with a connected MuPix10 insert PCB is shown in Figure 21.

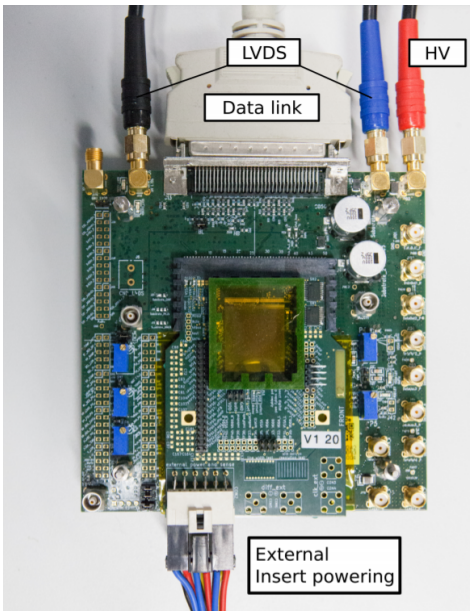

Figure 21: Motherboard with connected MuPix10 insert PCB.

4.4 FPGA

A Field-Programmable Gate Array (FPGA) is a integrated circuit consisting of configurable logic elements. It is often used to flexibly design and test complex logic circuits. In this setup, the Stratix IV GX FPGA Development Board [14] is used for the readout of MuPix10. On the one hand, the FPGA provides the chip configuration as well as the reference clock for the sensor. On the other hand it receives and processes the serialized MuPix10 data and forwards it via a PCIe connection to the data acquisition computer.

4.5 DAQ

The data coming from the FPGA is further processed on a desktop PC. This combination is referred to as the Data Acquisition (DAQ) system. For this thesis, a single sensor version of the MuPix Telescope DAQ system is used, which provides

a fast readout of the sensors data together with an graphical user interface in order to monitor and control measurements. A more specific description of the MuPix Telescope DAQ system is given in [15].

Part III

Calibration

5 Calibration Methods

The production of integrated circuits at the nanometer scale requires a very high precision in the fabrication process. Even though recent photolithograpic and chemical processes provide a very good accuracy, there are still slight variations within the electric components. This limitation in precision also affects the signal generation and processing of the MuPix sensors, which was discussed in Section 4.1.1 and, therefore, leads to signal variations from pixel to pixel. These can manifest, e.g., in the size or timing of the signal, as well as in the electronic noise. In order to achieve a more uniform response of the pixels, different calibration methods can be performed on a sensor. The choice of the calibration method to adopt depends on the requirements of the experiment or the measurement to be performed. In the following sections, different approaches for the MuPix10 calibration will be described and discussed.

5.1 Signal Tuning

The method of signal tuning aims for a uniform distribution of pixel thresholds across the sensor. The following sections provide an overview of the important characteristics and tools of the signal tuning as well as on the tuning procedure itself.

5.1.1 S-curves

The number of hits detected by a pixel using a fixed input signal as a function of the comparator threshold follows a characteristic shape. Given an ideal sensor without any noise, no hits will be detected if the threshold exceeds the voltage height of the signal. If the threshold is lower than the signal height, all incoming hits are detected with a probability of one. This leads to a Heaviside function for the detection probability as shown in Figure 22a.
However, a real signal has also a Gaussian noise component which leads to a smoother s-curve shape. This s-curve can be described as shown in Equation 13 using the Gaussian errorfunction $erf(x)$.

$$f(x) = \frac{1}{2}\left(1 - erf\left(\frac{x-\mu}{\sqrt{2}\sigma}\right)\right) \tag{13}$$

This equation relies on two free parameters: the mean μ and the standard deviation σ. Here, μ is the threshold value which corresponds to a detection probability of 0.5. It is also called the pixel threshold and is the characteristic variable for the signal tuning method. The deviation σ is directly correlated to the noise and can be used as a characteristic value for its quantification.

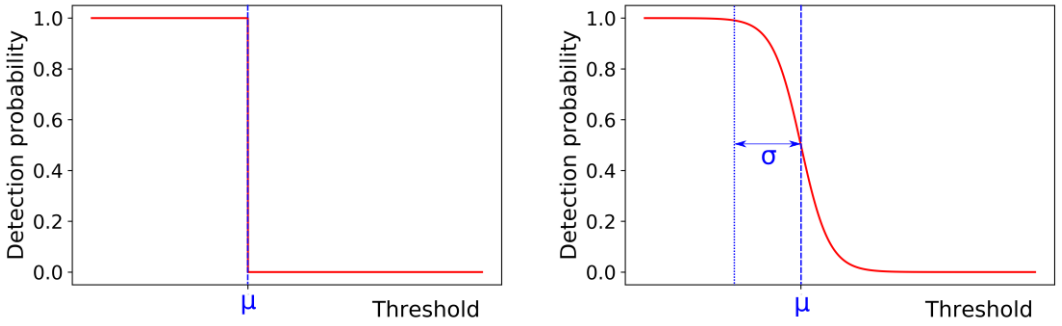

(a) Ideal s-curve.

(b) Realistic s-curve with noise component.

Figure 22: Noise influence on s-curves.

5.1.2 Stable s-curve fitting

Since the method of signal tuning requires a reasonable precise fit of each pixel's s-curve, it is necessary to use a efficient and stable fitting algorithm working independent of different input parameters of the threshold scan. In this thesis, an algorithm for this task was developed using CERN's data analysis package ROOT based on the programming language C++.
The fit of a single threshold scan for one pixel is performed using Equation 13 as already described in Section 5.1.1. In order to achieve a stable fitting procedure, initial prefit parameters for μ and σ have to be provided. In the interest of a more generic algorithm usable for the fit of 64.000 slightly varying s-curves, these initial parameters are directly determined from the raw data. Once an s-curve is measured, its discrete differential is analyzed, which follows a Gaussian distribution. For this thesis, the derivative of the s-curve is always negative, which results in a negative Gaussian distribution. Its mean and standard deviation are equivalent to the s-curve parameters and are therefore taken as starting parameters for the s-curve fit. This method has the advantage that Gaussian distributions are generally easier to fit numerically than s-curves. An example of a measured s-curve and its corresponding discrete derivative is given in Figure 23.
However, for a stable fitting performance, the Gaussian distribution itself also requires initial fit parameters for μ, σ and its scale A. As a first estimation, it is sufficient to use the minimum value of the distribution for A and its bin position for μ. The standard deviation is estimated by calculating the difference between

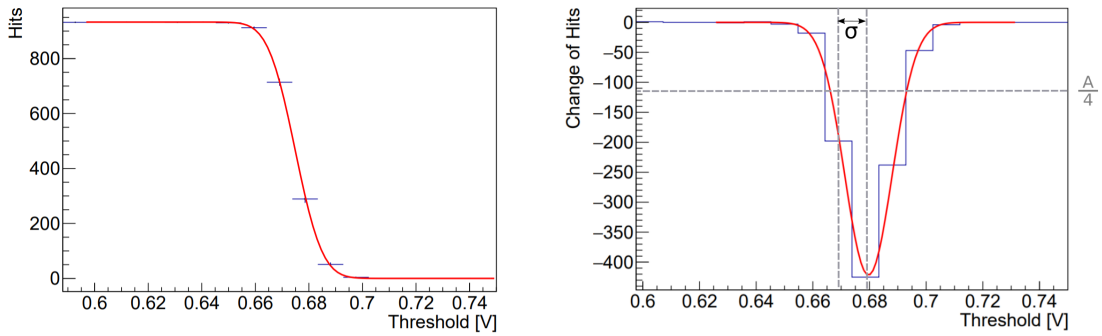

(a) Example of a fitted s-curve.

(b) Example of a calculated s-curve derivative.

Figure 23: Determination of s-curve prefit parameters

mean and the closest bin position at which the value of the distribution is one quarter of the minimum value.
Additional to the prefit parameters, a suitable fit range of the s-curve has to be found. Here, the upper limit is simply set to the first data point, since the higher value of all threshold scans is set to a point where no hits are registered. However at low threshold, the pixel noise can step in and become a dominant component of the s-curve. This effect should appear at a much lower threshold value than the mean of the s-curve, leaving a plateau between the s-curve and the noise curve. This behaviour is illustrated in Figure 24. Therefore, a lower limit of the fit has to be set at a point on the plateau before the noise curve affects it. To ensure this, the upper limit of the plateau is set to $3\,\sigma$ below the s-curve mean. From this point downwards, the difference between each value and the previous one is checked. Once this difference exceeds 10 % of the value at the upper limit of the plateau, or if it stays constant for $2\,\sigma$, the lower limit of the plateau is set. This value is also used as the lower boundary of the fit range. Averaging the values between upper and lower limit of the plateau also leads to the prefit parameter of the s-curve's scale.
This method of fitting allowed to reliably obtain the necessary values for the signal tuning.

5.1.3 Signal tuning procedure

In order to perform the signal tuning, the influence of the TDAC value on the pixel threshold μ of every pixel has to be known. As described in section 4.1.3, the TDAC dependency is expected to decrease linear. Its slope A can be easily determined using a linear fit and describes the tuning voltage per TDAC step. This is illustrated in Figure 25.
Before the actual tuning process starts, the untuned state of the sensor is charac-

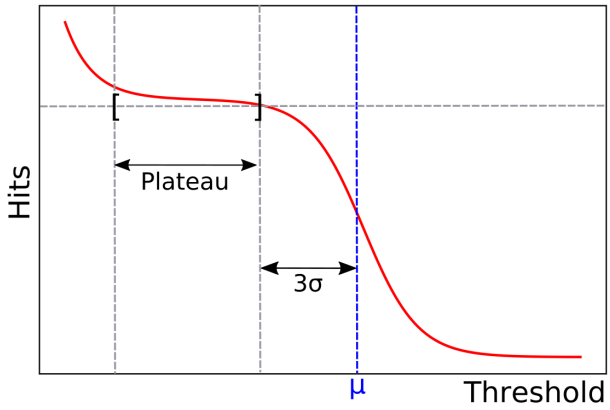

Figure 24: Illustration of the plateau fit.

terized. The initial distribution of pixel threshold can be described by a Gaussian. Since pixel thresholds can only be decreased on MuPix10, the target threshold $\bar{T}$ of the tuning procedure is given by the lowest pixel threshold observed on the sensor. This pixel will remain untuned (TDAC=0) during the procedure, while the other pixels are tuned towards $\bar{T}$. The threshold voltage decrease ΔThr for one pixel needed in order to reach $\bar{T}$ is given through the difference of pixel and target threshold:

$$\Delta Thr = \mu - \bar{T} \tag{14}$$

From ΔThr, the corresponding TDAC value has to be derived. This value can be directly determined from the pixels TDAC dependency by dividing the needed voltage decrease by the TDAC slope A as shown in Equation 15. Since the TDAC value is digital, the calculated fraction has to be rounded to the closest integer value.

$$TDAC = \left\lfloor \frac{\Delta Thr}{A} + \frac{1}{2} \right\rfloor = \left\lfloor \frac{\bar{T} - \mu}{A} + \frac{1}{2} \right\rfloor \tag{15}$$

Calculating and applying the TDAC value for each pixel should lead to a Gaussian pixel threshold distribution centered around the target threshold. Compared to the initial distribution of μ, the tuned distribution should not only be shifted but also narrowed around $\bar{T}$.

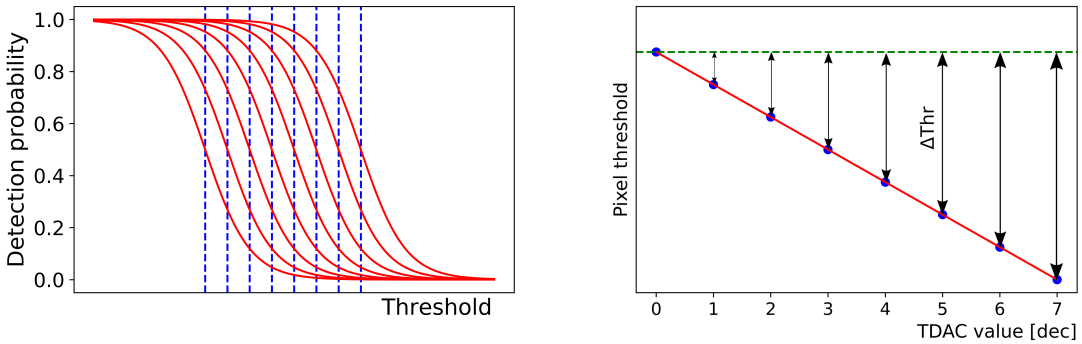

(a) Sketch of the TDAC influence on s-curves. With higher TDAC values, the mean of the s-curves decreases.

(b) Sketch of the threshold-TDAC dependency.

Figure 25: Expected TDAC influence on the pixel threshold.

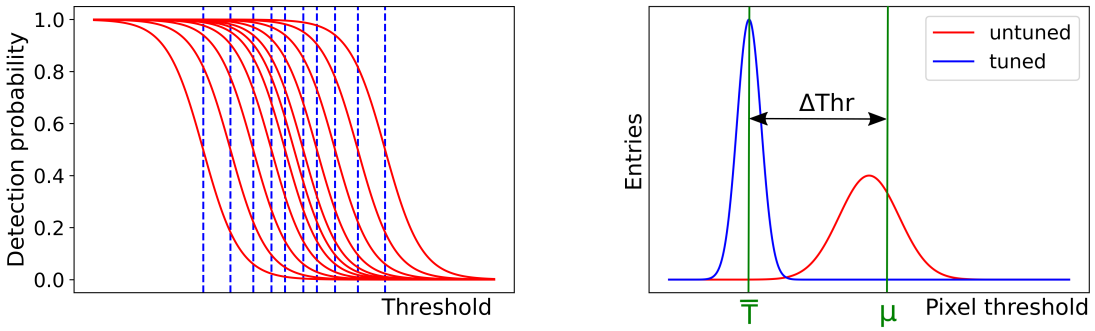

(a) Sketch of the s-curve distribution of different pixels across the sensor.

(b) Sketch of the signal tuning procedure.

Figure 26: Signal tuning procedure.

5.2 Noise Tuning

The main goal of the noise tuning is to achieve a uniform noise response across the pixel matrix. The implementation of noise tuning does not require the use of injection signals or external radiation sources. The following sections provide an overview of the method.

5.2.1 Noise curves

The threshold dependency of a pixels noise rate follows an exponential-like behaviour. With lower threshold, more and more noise fluctuations will be registered as a hit, which leads to an increasing noise rate f_{noise}. A high noise rate might

compromise the track reconstruction with false hits and complicates the following data analysis. Therefore, in many applications tight restrictions are set on pixel noise rate, which is required to be below a certain maximum value f_{max}. For the scope of this thesis, the threshold, at which the noise rate f_{noise} exceeds f_{max} is called Thr_{noise}. This threshold is subject to interpixel variations and is the characteristic value for the noise tuning procedure. A sketch of the noise dependency is given in Figure 27.

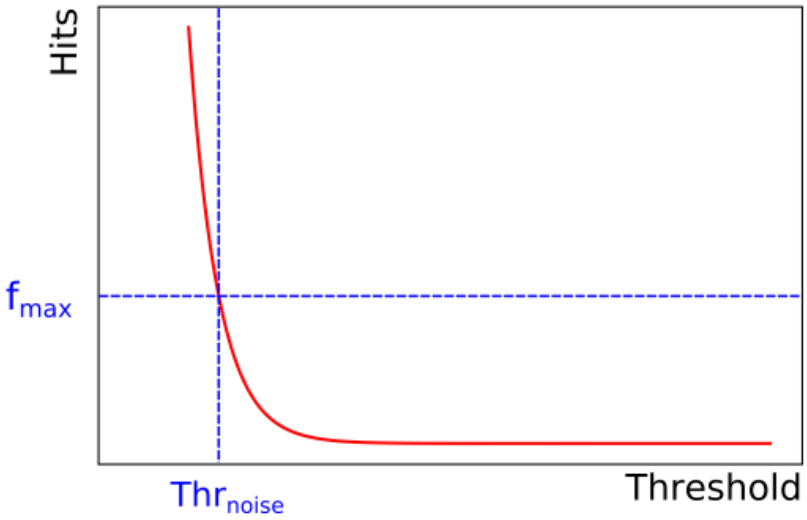

Figure 27: Determination of Thr_{noise}.

5.2.2 Noise tuning procedure

The noise tuning procedure works similar to the signal tuning method discussed in Section 5.1.3. Again, the first step is to determine the TDAC dependency of Thr_{noise}, which is also expected to be linear as shown in Figure 28. The initial, untuned distribution of Thr_{noise} is measured and a target threshold $\bar{T}$ is chosen at its lower end. Now, the threshold difference ΔThr between $\bar{T}$ and the Thr_{noise} of each pixel can be calculated. With the slope information of the TDAC dependency, the corresponding TDAC value can be calculated analogously to Equation 15. As a result of applying the chosen TDAC values, the initial Thr_{noise} distribution should be narrowed around $\bar{T}$. An illustration of this is shown in Figure 29.

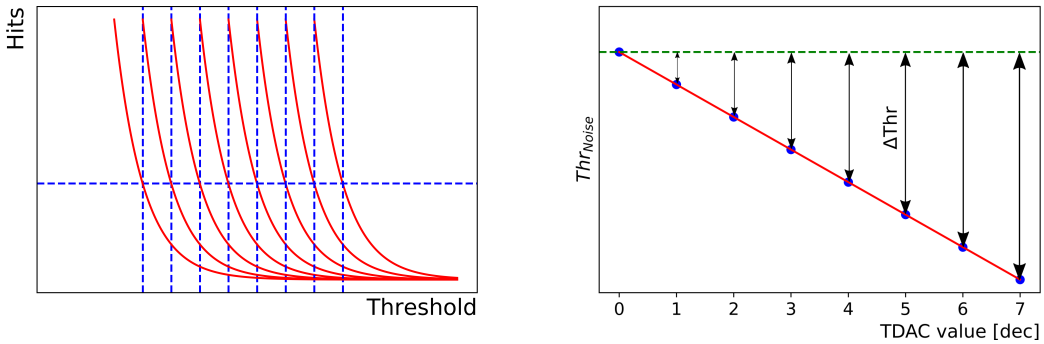

(a) Expected TDAC influence on the noise curves. With higher TDAC values, the curves shift to lower thresholds.

(b) Sketch of the expected Thr_{noise}-TDAC dependency.

Figure 28: Expected TDAC influence on the noise.

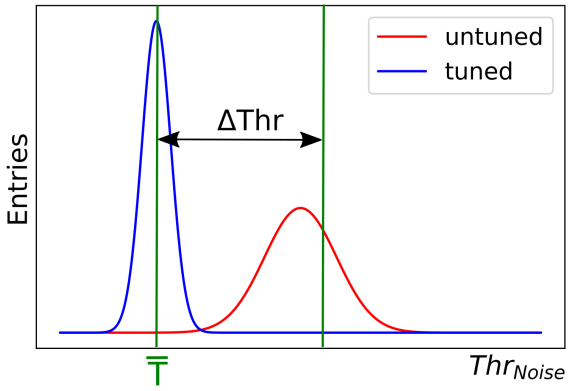

Figure 29: Illustration of the noise tuning procedure.

5.3 Timing Tuning

The last tuning method which is discussed within this thesis is the so called timing tuning. Its goal is to a achieve a uniform signal propagation delay across the pixel matrix. This uniformity should lead to an improvement of the sensors time resolution. In the following sections, an overview of the method is given. Furthermore, its possible implementation on the MuPix10 is shortly discussed.

5.3.1 Latency

The latency λ describes the signal propagation delay of a pixel and is the characteristic value of the timing tuning. It represents the time difference between an

incoming signal and the registration of it by the comparator. For the registration of timing information, a MuPix10 hit contains the timestamp information Hit_{TS}, which corresponds to the value of an internal fixed-clock counter at the time the hit was registered. To compute the hit latency, another timestamp must be used: the injection timestamp Inj_{TS}. This timestamp refers to the time frame in which charge is injected into the sensor diode. A picture of this is given in Figure 30.

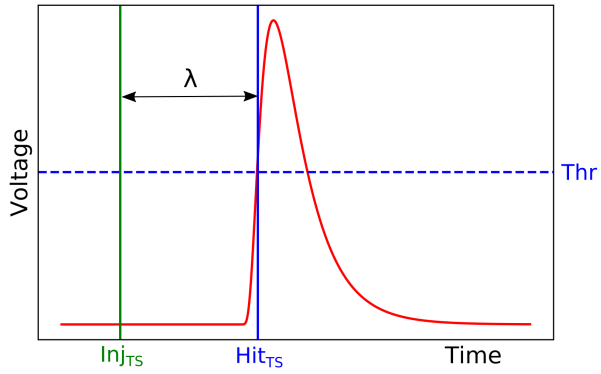

Figure 30: Definition of the latency.

Now, the latency is simply defined as the time difference between the injection- and the hit-timestamp.

$$\lambda = Inj_{TS} - Hit_{TS} \tag{16}$$

However, variations in the analog cell of the pixel lead to different shapes of the signal pulse. Those differences may affect the signal's hit-timestamp. For instance, a deviation of the baseline can influence Hit_{TS} as shown in 31a. Another example is the is the variation of the signal's rise time RT occurring due to variations within the signal amplifier. Its effect on Hit_{TS} is illustrated in Figure 31b.

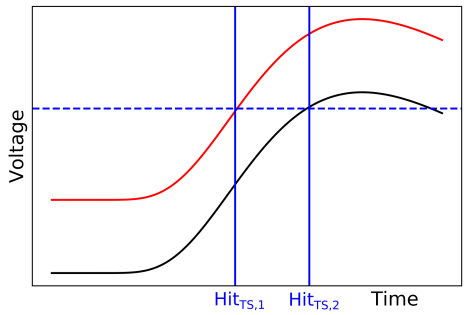

(a) Baseline influence on Hit_{TS}.

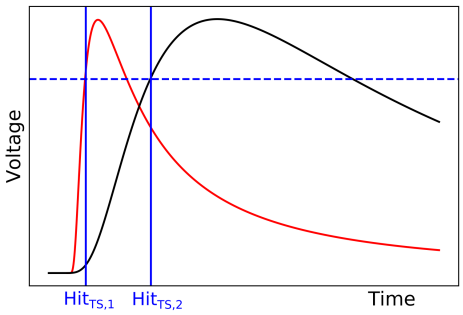

(b) Risetime influence on Hit_{TS}.

Figure 31: Possible effects leading to interpixel variations of the latency

5.3.2 Timing Tuning Procedure

The possibility of adjusting the threshold with TDACs can also be exploited in order to correct for latency variations. For example, if the threshold is increased, the signal exceeds the threshold voltage later. This results into a higher latency. The effect can be seen in Figure 32a. Similar to the other tuning mechanisms, the latency-TDAC dependency can be measured for each pixel. Again, the TDAC values can be determined analogously to Equation 15.

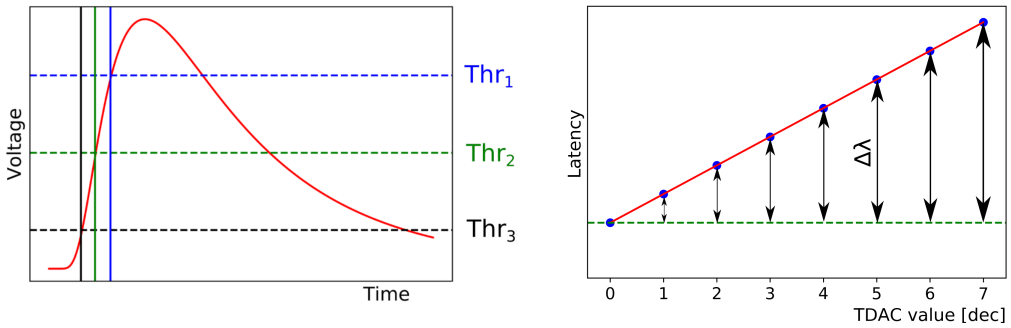

(a) Threshold influence on Hit_{TS}.

(b) Sketch of the expected latency-TDAC dependency.

Figure 32: Tuning of the latency.

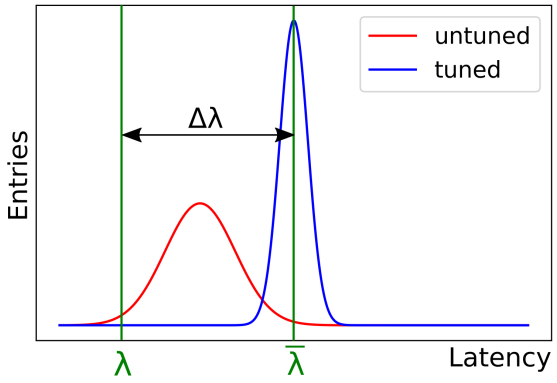

Figure 33: Illustration of the timing tuning procedure.

5.3.3 Timing Tuning on MuPix10

As already mentioned before, the main purpose of timing tuning is to decrease the latency variations across the pixel matrix and thus improve the overall time resolution of the sensor. The potential tuning effect on the latency with a certain adjustment of the threshold depends on the rise time RT of the pixel's signal. For

instance, we can consider two signals with different rise time, RT_{low} and RT_{high}, where the signal with RT_{low} is steeper than the signal with RT_{high}. In order to achieve the same latency correction $\Delta\lambda$, the threshold shift $\Delta Thr_{high\,RT}$ on the signal with RT_{high} has to be greater compared to the shift $\Delta Thr_{low\,RT}$ for the signal with RT_{low}. This correlation is illustrated in Figure 34.

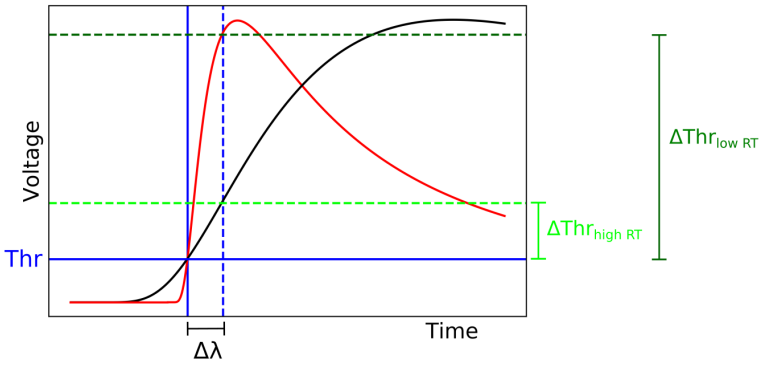

Figure 34: Comparison of needed threshold shifts for signals with high and low RT.

Since the rise time of the pixels on MuPix10 is designed to be as short as possible for a good time resolution, it might happen that the needed delay correction for the tuning requires a high increase in threshold. As a consequence, smaller signals might become undetectable, which lowers the sensors efficiency.
In order to estimate the impact for MuPix10, a rough calculation of the necessary threshold difference is carried out using data from MuPix8. Since from this sensor generation, no significant changes in the structure of the amplifier were implemented, this measurements can be used as a valid reference. All values for the following calculation are obtained from [16]. Here, the observed maximum delay over the sensor matrix were found to have a value of $\Delta\lambda \approx 60\,ns$. With an exemplary signal amplitude of $Amp \approx 200\,mV$ and a rise time of $300\,ns$ the necessary threshold adjustment ΔThr can be estimated following Equation 17. Here, the pulse is assumed to be triangular shaped.

$$\Delta Thr \approx \frac{Amp}{RT}\Delta\lambda = 40\,mV \tag{17}$$

At a first glance, this value seems not too high for a possible timing tuning. However, as aforementioned, latency corrections can only be applied increasing the local threshold. Also, the choice of applied latency corrections does not take noise or efficiency into account. If, after the application of tuning values, the global threshold is lowered until the pixel with the highest delay is directly above the maximum acceptable noise rate, the pixel with the lowest delay has to operate 40 mV above. Regarding Figure 35, a ΔThr of 40 mV can directly lead to a significant reduction of the sensor‘s efficiency. The same behaviour can also be expected

for MuPix10.

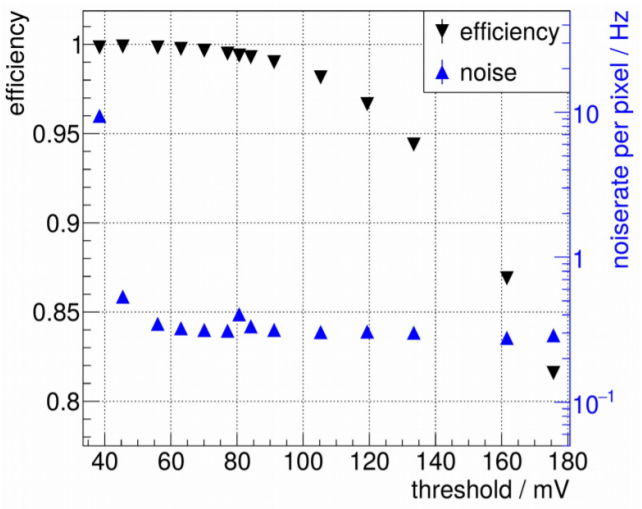

Figure 35: Hit efficiency and noise as a function of the threshold on MuPix8. Taken from [7].

In general, the MuPix sensors are designed for a precise and efficient particle tracking within the Mu3e detector, while scintillating tiles and fibers are responsible for precise timing measurements. For this reason, the study and implementation of timing tuning on MuPix10 is more of academic than of operational interest.

Part IV

Measurements

6 Power consumption of VPDAC

As already mentioned in Section 4.1.3, the tuning voltage and therefore the strength of the tuning directly depends on the value of VPDAC. In the following sections, the value of VPDAC is reported as a hexadecimal value unless otherwise stated. According to the Mu3e requirements, the MuPix10 sensor should not exceed a power consumption of 350 mW/cm^2 [7]. This value limits the maximum tuning current which may be applied to the detector. In order to receive an estimation of the sensors power consumption as a function of the tuning strength, the currents of the supply voltages I_{VDDA}, I_{VSSA} and I_{VDD} are measured in terms of VPDAC. The result is shown in Figure 36.

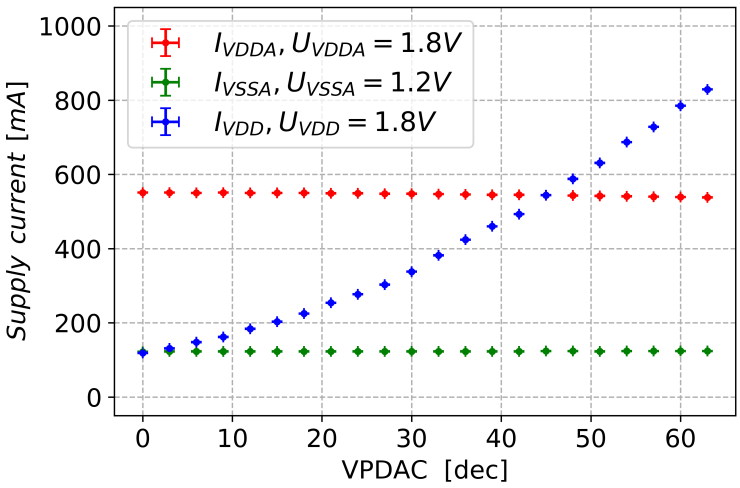

Figure 36: Supply currents as a function of VPDAC.

Here, one can clearly see that only I_{VDD} depends on VPDAC while I_{VSSA} stays unaltered. For I_{VDDA}, a small voltage decrease of about 10 mV is observed.
From the measured currents, the power consumption per area P can be estimated using Equation 37, where $A_{sensor} \approx 4\,cm^2$ is the area of the sensor.

$$P = \frac{U_{VDDA}I_{VDDA} + U_{VSSA}I_{VSSA} + U_{VDD}I_{VDD}}{A_{sensor}} \tag{18}$$

By applying this to the dependency of the currents on VPDAC, the plot in Figure 37 is obtained. From this plot it can be inferred that the Mu3e requirements on power consumption set a maximum value for VPDAC of 8 on the used setup

configuration. However, during the analysis of this thesis a configuration problem on the insert PCB was found leading to a significant increase of the VDDA current of about 400 mV [17]. Correcting the measured power consumption with this estimation leads to a much higher possible tuning range up to a value of VPDAC=0x2D. A plot of the relative increase of the power consumption is given in Appendix A.1.

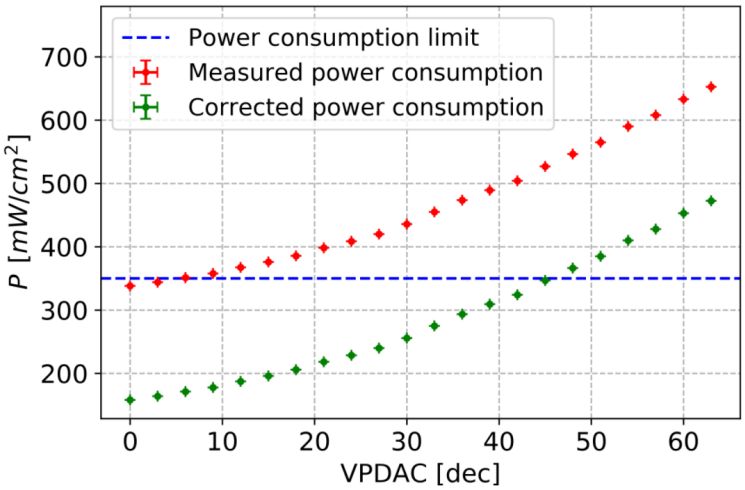

Figure 37: Observed and corrected power consumption as a function of VPDAC.

7 Signal tuning

The following sections contain all measurements which were carried out in order to perform and fulfill the signal tuning method. Furthermore, the observed experimental limitations are investigated.

7.1 Injection limitations

Test pulse injection, which is explained in Section 4.1.4, is chosen as the input method for the signal tuning due to its capability of providing sharp, mono energetic signals at high frequencies. However, during the first s-curve measurements on MuPix10 it was observed that the number of simultaneous injected pixels affects the pixel threshold distribution. In order to investigate this effect, a s-curve measurement for differently sized injection quadrants was carried out using an injection voltage of 1.8 V. Observing the s-curve of one pixel for different total injection areas, as shown in Figure 38, two effects are visible. On the one hand, the s-curves shift towards smaller thresholds with higher injection areas, while on the other hand, the standard deviation of the curves increases.

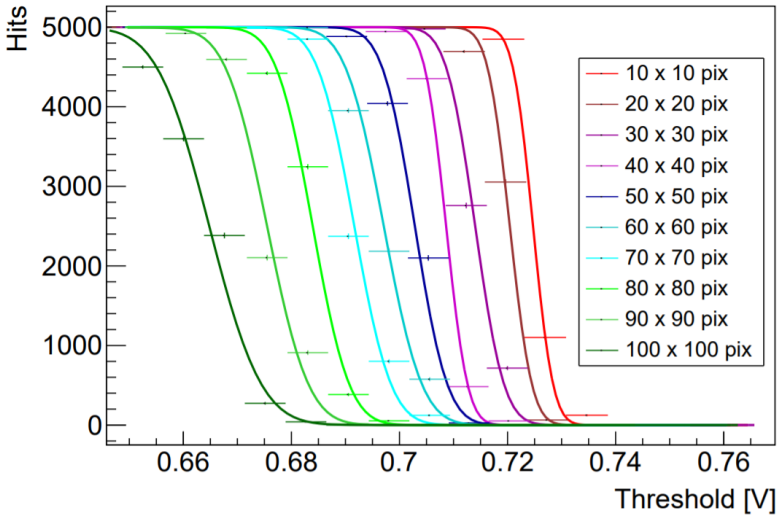

Figure 38: S-curves for injection areas from 10×10 pix to 100×100 pix. With higher injection areas, the mean of the curves shifts towards lower thresholds while their standard deviation increases.

For the initial area of 10×10 pixels, the pixel threshold distribution as well es the

distribution of the standard deviation of the s-curves were fitted with a Gaussian distribution. The resulting mean values on this initial area together with their fitting errors are plotted against the total injection area in Figure 39.

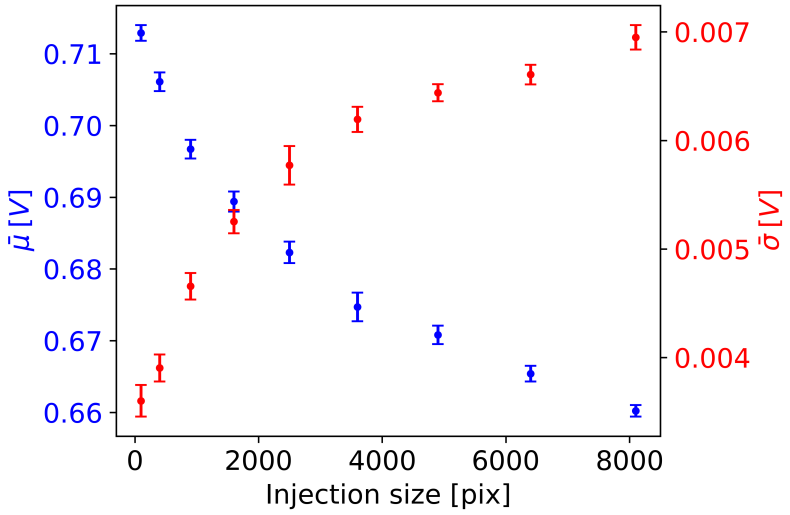

Figure 39: Mean $\bar{\mu}$ of the pixel threshold distribution and the mean $\bar{\sigma}$ of the standard deviation distribution for different injection areas.

If one considers the distribution of the injection voltage on MuPix10, which was described in Section 4.1.4, one clearly sees that a higher injection area leads to an increasing total injection capacitance. A possible reason for the decreasing pixel threshold could therefore be an insufficient charging of the capacities due to a limited injection current. An insufficient charging would lead to a smaller amplitude of the injected signal. As a further check, the signal amplitude generated using injection was measured as a function of the area. Figure 40 shows the measurement for the same quadrants as used before. The curve shows, that the pulse height decreases almost linear up to an injection area of 10.000 pix. Using a linear fit, the decrease of the amplitude was found to be around 9 mV/100 pix within this range. The increase of σ with higher injection areas shown in Figure 39 is therefore most likely a result of this amplitude decrease.
Furthermore, the influence of the used injection voltage on the signal amplitude of pixel (0,0) was measured for different shapes of the injection area. The result can be seen in Figure 41. First, the measurement was carried out using just one double pixel. Up to an injection voltage of 0.7 V, the increase of the amplitude is approximately linear. With higher voltages, the amplitude saturates at a value of $\approx$ 290 mV. Second, the injection area was increased to one full double column (2×250 pix). This measurement showed within the statistical errors the same behaviour as for the double pixel. However, the measurement was also repeated for two full rows of the sensor (256×2 pix). Using this injection area, the signal ampli-

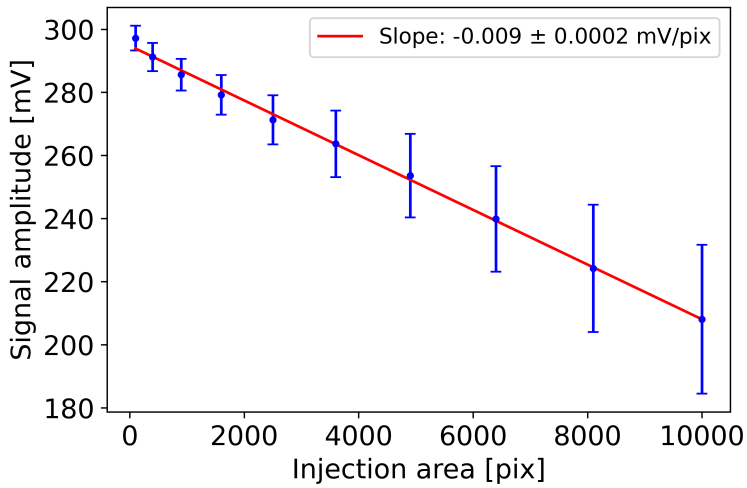

Figure 40: Dependency of the signal amplitude on the injection area.

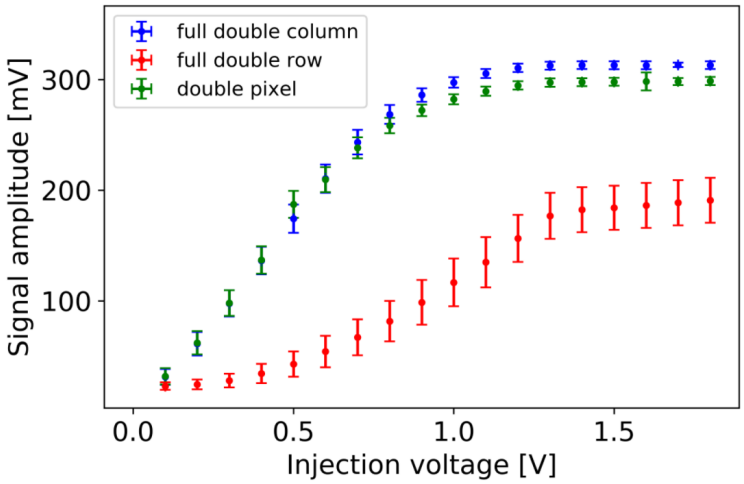

Figure 41: Dependency of the signal amplitude on the applied injection voltage for a full double column, a full double row and a double pixel.

tude was overall smaller than in the measurements before. The curve now shows a non-linear increase and starts saturating from an injection voltage of $\approx 1.3\,\mathrm{V}$ at an amplitude of $\approx 180\,\mathrm{mV}$. This behaviour shows that the injection limitation not only depends on the used area, but also on the area shape. Considering the injection routing shown in Figure 19, the most likely reason for this is a voltage drop along the column distribution.

7.2 Determination of VPDAC

In advance of the signal tuning procedure, the strength of the tuning has to be determined. Therefore, a VPDAC value has to be chosen, which must be on the one hand high enough to tune all pixels sufficiently, while on the other hand, it should be chosen as low as possible in order to keep the power consumption within requirements, or even lower if possible. For this reason, the pixel threshold distribution at the highest TDAC value of 7 was measured for increasing values of VPDAC. In this case, the distributions were not measured taking the full sensor into account. A grid of 25×25 pixels evenly distributed over the whole sensor was used. As exemplary shown in Figure 42, the resulting distributions were compared to the untuned (TDAC=0, VPDAC=0) distribution of the sensor.

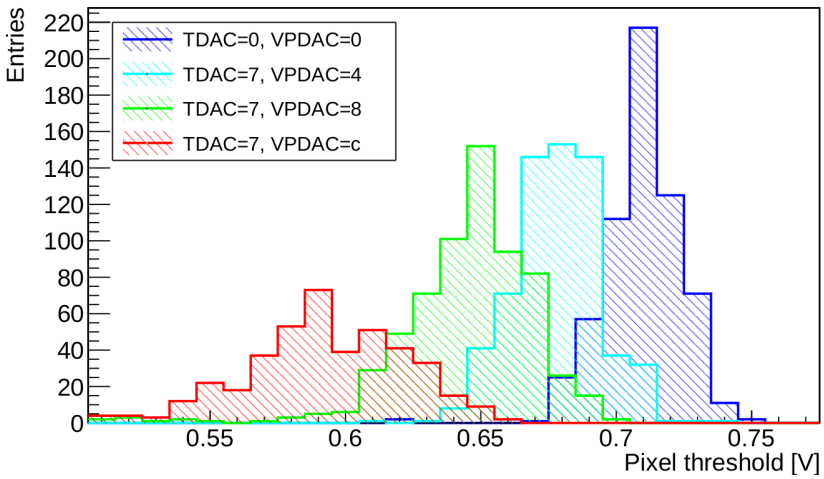

Figure 42: Pixel threshold distribution for different values of VPDAC.

Here, one already sees two effects of the tuning on the s-curves. First, the pixel thresholds μ are lowering with higher tuning strength just as expected by design. Secondly, the standard deviations σ of the s-curves are increasing, which is most likely a result of pixel variations of the tuning influence. In order to investigate this effect, μ and σ distributions of the s-curves for each VPDAC measurement were fitted with a Gaussian distribution. The results are depicted in Figure 43. A certain VPDAC value is regarded as sufficient for the tuning if it is able to shift the pixel threshold distribution completely on the left of the untuned one. This ensures that the pixel which has the highest initial pixel threshold can be tuned to the target threshold, i.e. the lowest threshold value observed in the untuned distribution. With the assumption that the relative position of a pixel threshold within a distribution does not change significantly with higher VPDAC values, a small overlap between initial and tuned distribution is acceptable. Following this criteria, a value of VPDAC=0xA is found to be most suitable. A comparison can be seen in Figure 44.

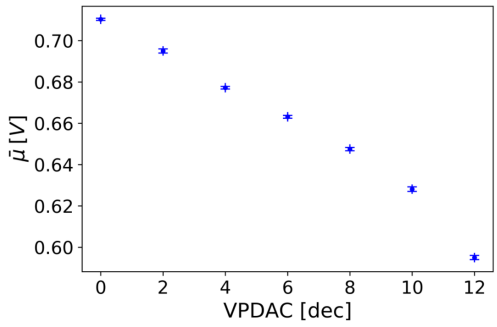

(a) Mean of the pixel threshold distribution in dependence of VPDAC.

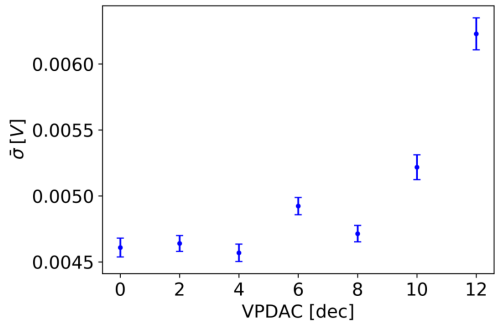

(b) Mean of the sigma distribution in dependence of VPDAC.

Figure 43: VPDAC influence on s-curves.

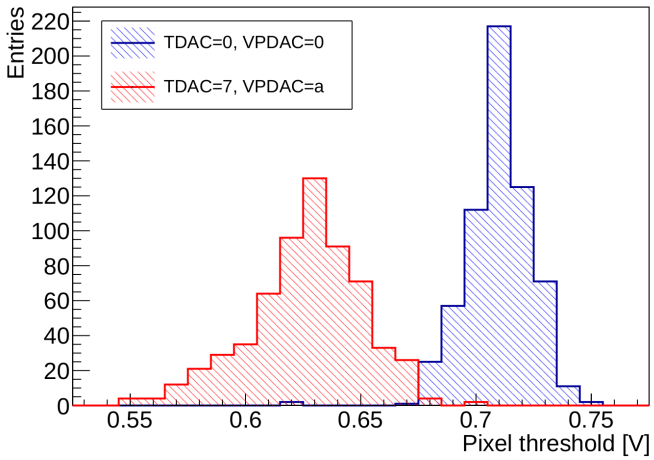

Figure 44: Shift of the pixel threshold distribution for VPDAC=0xA.

7.3 Signal Tuning on a sensor subdivision

Due to the limitations on the injection area described in Section 7.1, the signal tuning was first performed on a smaller subdivision of the sensor. Here, a quadrant with a size of 50×64 pixels was chosen for tuning.
As a first step, the influence of the TDAC values on the pixel thresholds (threshold-TDAC dependency) was investigated. Therefore, the s-curves of all pixels in the tuning area were measured and fitted varying the TDAC value from 0 to 7. As an example, the measured s-curves and the corresponding pixel thresholds are shown in Figure 45 for one pixel. The threshold-TDAC dependency was found to be uniform and linear for all pixels just as intended per design. A 2-dimensional plot of pixel threshold distributions against TDAC values is shown in Figure 46a. The slope of the dependency directly corresponds to the tuning strength A described in Section 5.1.3. The TDAC slope distribution, which can be seen in Figure 46b, was found to be Gaussian distributed around a value of 12 mV. With an RMS

of 1.5 mV, this leads to a relative error of about 12.5 %. This spread most likely lead to the in Section 7.2 observed increase of the pixel threshold distributions standard deviation with higher VPDAC.

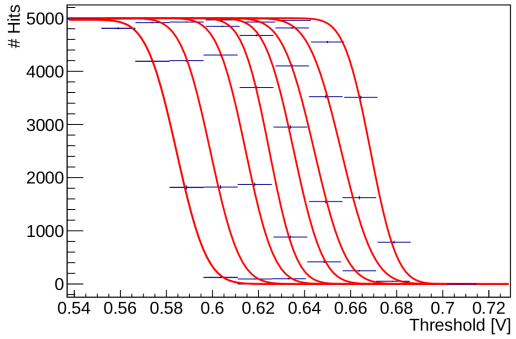

(a) S-curves of pixel [0,0] for all TDAC values from 0 (right curve) to 7 (left curve).

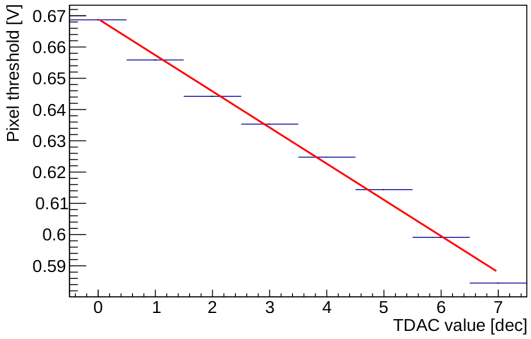

(b) Pixel threshold of pixel [0,0] in dependence of VPDAC

Figure 45: TDAC influence on s-curves.

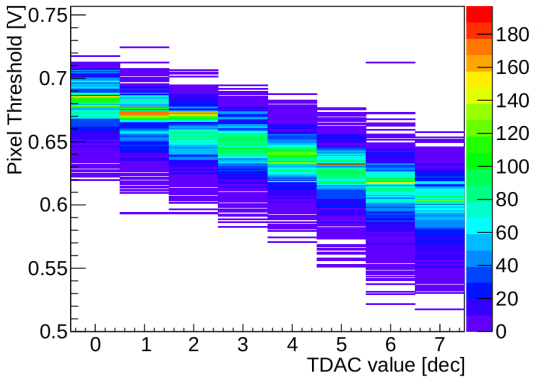

(a) Pixel threshold distributions in dependence of the TDAC values for all pixels in the tuning area.

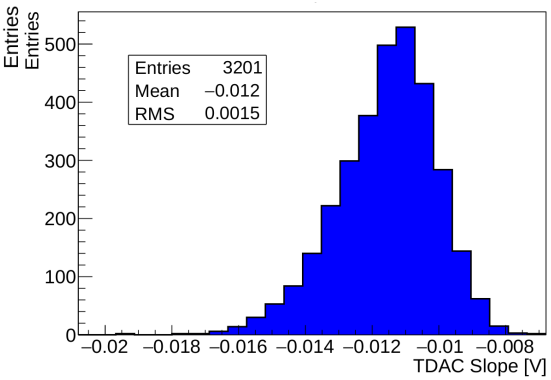

(b) Distribution of the TDAC slopes across the sensor matrix.

Figure 46: Investigation of the threshold-TDAC dependency.

From the initial distribution, the target threshold was determined to a value of 630 mV. With this information, the TDAC value for every pixel was calculated according to Equations 14 & 15. The resulting distribution of chosen TDAC values together with the spatial distribution is shown in Figure 47. The TDAC distribution shows a Gaussian distribution which in general implies a suitable set of chosen TDAC values. However, an ideal distribution would be symmetric and centered around a value of 3.5, while the observed one shows a mean value of 4.34 and is therefore slightly asymmetric. From this it can be concluded that VPDAC can be chosen higher than VPDAC=0xA in order to improve the tuning

further. Plotting the value of TDAC for every pixel in a 2-dimensional histogram, as shown in Figure 47b, the TDAC values appear to be randomly distributed across the tuning area. This behaviour is expected from random variations across the pixel matrix and therefore indicates a reasonable TDAC set. The application of this set results in the tuned pixel threshold distribution, which can be seen in Figure 48.

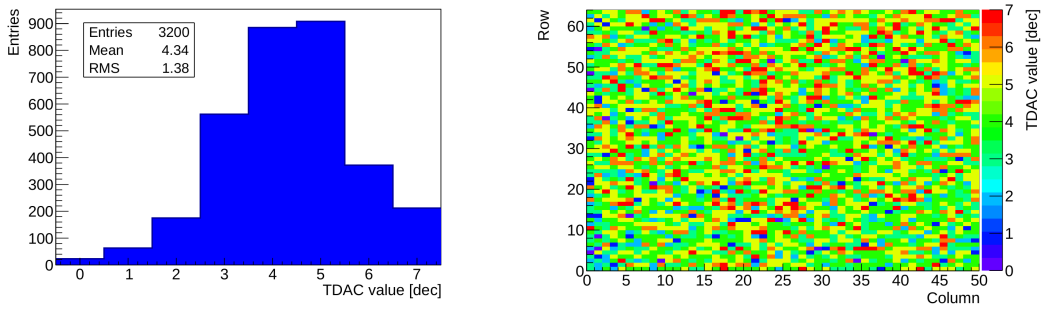

(a) Distribution of the chosen TDAC values.

(b) Spatial distribution of the chosen TDAC values.

Figure 47: Determined TDAC values according to the signal tuning method.

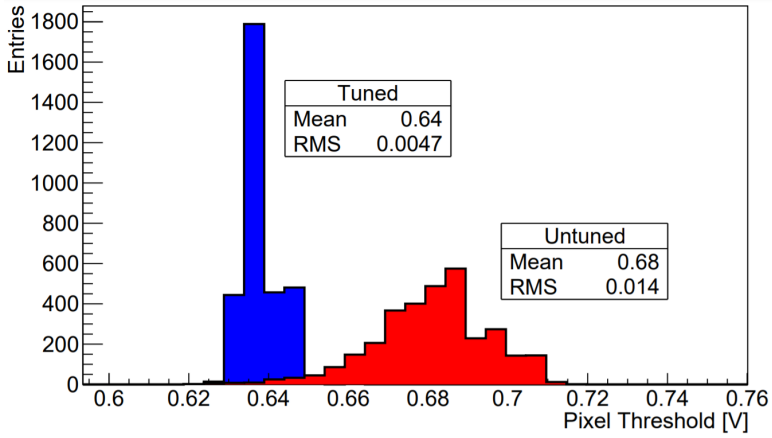

Figure 48: Comparison between the initial and tuned pixel threshold distribution on the sensor subdivision. Already published in [7].

Here, one can clearly see that the initial pixel threshold distribution with a mean of 680 mV, was shifted towards a lower mean of 640 mV. This is 10 mV above the chosen target value of 630 mV. More important, the RMS of the distribution is narrowed significantly from a value of 14 mV, to a value of 4.7 mV. Therefore, the signal tuning of the subdivision can be regarded as successful. The results are discussed in Section 9.1.

7.4 Signal Tuning on the full sensor

After the feasibility of the signal tuning method has been verified in Section 7.3, its extension to the full sensor was implemented. Due to the injection area limitation discussed in Section 7.1, the pixel matrix is divided in small portions which are injected separately, a procedure named "part-by-part" tuning. Since a loss of signal amplitude was observed with the injection of a full row of the sensor, a vertical division into 32 stripes with a size of 8×250 pix is chosen to minimize the amplitude loss. An illustration of the chosen division is given in Figure 49.

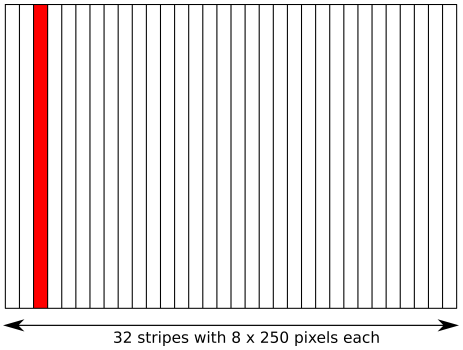

Figure 49: Illustration of the pixel threshold measurement using injection stripes.

Using this method, the pixel thresholds for the full sensor matrix are determined for each TDAC value. The measured pixel threshold map for TDAC=0 is shown in Figure 51a. Here, a clear spatial dependence is observed. First, the distribution shows a positive gradient along the column axis. Additionally, there a dip within the row dimension is visible. Most likely, this effect occurs due to losses within a yet unspecified voltage distribution. However, the observed pattern does neither match the injection nor the threshold routing on the sensor.
Analog to the signal tuning on a sensor subdivision, a set of TDACs is calculated. Its distribution is shown in Figure 50. Here, the distribution is also Gaussian shaped with a mean value of 3.22, which indicates a slight increase in VPDAC could be applied for further tuning improvements. In contrast to the tuning on the sensor subdivision, the chosen TDAC set now also shows a clear spatial dependence. This is illustrated in Figure 50b. In this case, the choice of TDAC values directly matches the pattern of the untuned map. Pixels with a low pixel threshold compared to the rest are set to rather small TDAC values, while the pixels in the top and bottom of the pixel matrix are set to higher TDAC values.
The result of the tuning is depicted in Figure 51 & 52. This time, the mean of the pixel threshold value was lowered from a value of 730 mV to 710 mV. For the RMS, a significant decrease from 11 mV to 4.8 mV was achieved. This result is compatible with the result on the matrix subdivision and shows that the signal tuning works on the whole matrix. This result is also discussed in Section 9.1.

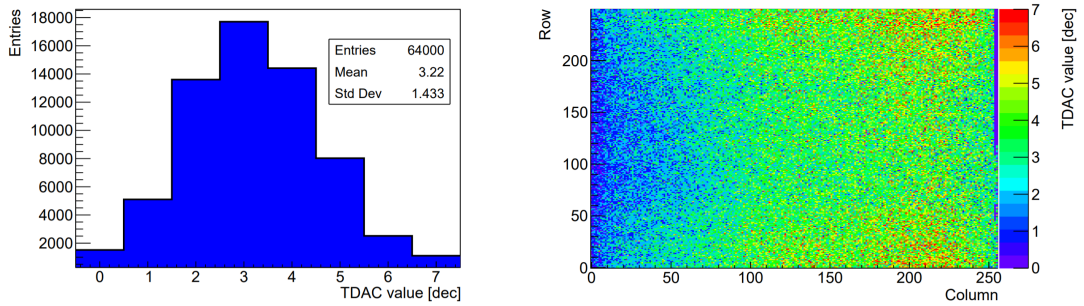

(a) Distribution of the chosen TDAC values.

(b) Spatial distribution of the chosen TDAC values.

Figure 50: Determined TDAC values for the full sensor tuning.

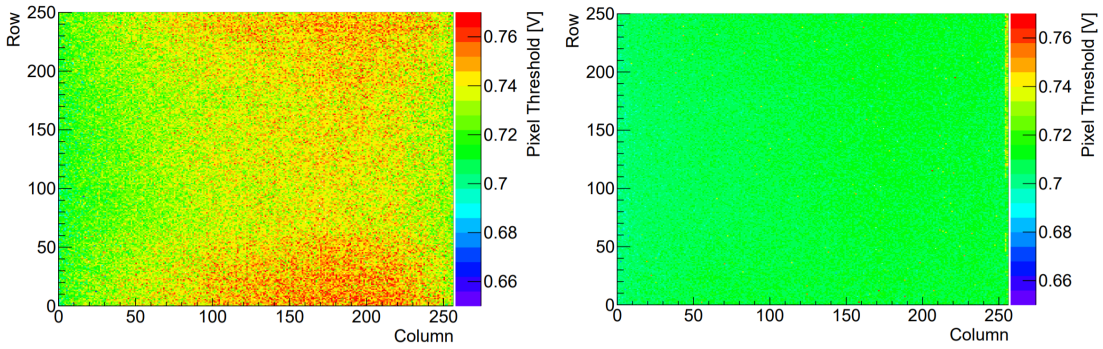

(a) Untuned pixel threshold distribution.

(b) Tuned pixel threshold distribution.

Figure 51: Comparison between the spatial pixel threshold distribution before and after the signal tuning.

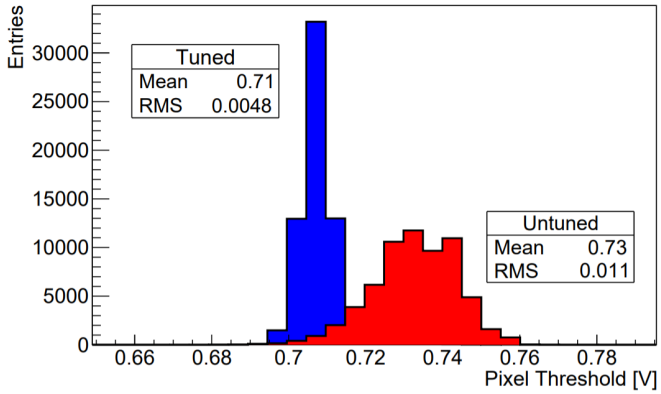

Figure 52: Comparision between the initial and tuned pixel threshold distribution on the full sensor.

8 Noise tuning

The following sections provide an overview of the limitations and the observed measurements on the noise tuning method.

8.1 Readout limitation

The readout of hit information in MuPix10 is performed using the so-called column drain readout method. For this, two physical pixel columns are assigned to one digital readout column. Here, all pixels within a digital column are connected to one databus. For each digital column, the readout cycle now starts from the beginning of the column and checks for hit information. If a hit is found, the hit information will be loaded into the databus and the pixel cell is reset. Then, the readout cycle starts again from the beginning of the column, without checking for further hits, and proceeds until the next hit is loaded or the end of the column is reached.
However, if a pixel gets noisy with a higher rate than the loading rate of the bus, the readout cycle will keep loading a hit from the noisy pixel. As a result, the following pixels in the column will never be read out. A sketch of this readout scheme is shown in Figure 53.

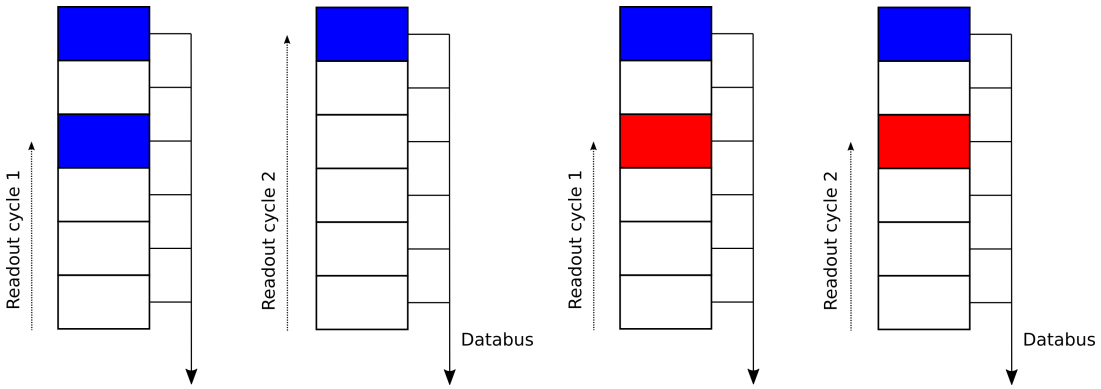

(a) Sketch of the column drain readout. Pixels are read out from one side of the column. Pixels with hit information (blue), will load their signal into the databus. Afterwards, the readout cycle repeats until all hits are registered.

(b) Sketch of the readout saturation. A noisy pixel (red) loads hit information into the databus. Due to high noise rates, it will again send hit information in the second cycle. Therefore it prevents the following pixels from being read out.

Figure 53: Sketch of the column drain readout with and without saturation

8.2 Successive Pixel masking

Due to the readout limitation discussed in Section 8.1 and the generally high rates of noise, it is not possible to receive noise curves of many pixels simultaneously. Therefore, during a noise scan, successive pixel masking is applied. In this procedure, a noise rate of 100 Hz/pix is defined at which a pixel can start to affect the readout. If during a threshold scan a pixel exceeds this rate, it will be masked as outlined in Section 4.1.3. In order to make sure that the noisy pixel has not blocked the readout of other pixels, the measurement for the current threshold is retaken. If no new noisy pixels appear, the next lower threshold is measured. This process continues until every pixel on the matrix is masked and all noise curves are measured. A sketch of the principle is shown in Figure 54.

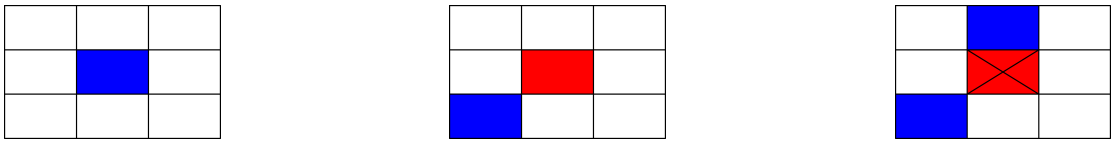

(a) (b) (c)

Figure 54: Principle of the successive pixel masking. At a relative high threshold (a), only one pixel shows hits. With a lower threshold (b), more pixel receive hits while initial pixel (red) now shows a noise rate which could affect the readout. In (c), the pixel gets masked and the same threshold is remeasured. Now, other pixels which were blocked before can send data.

8.3 Step size limitation

During the first noise curve measurements it was observed that even with very low thresholds noise curves of many pixels did not appear. A possible reason for this could be a too high threshold step size compared to the steepness of the curves. As shown in Figure 55, the step size should be lower than the noise fluctuation of the baseline. However, with a too high step size it might happen that from one step to the next, the threshold changes from above to below the baseline. In this case, the comparator stays always on and no hits can be registered any more. The designed threshold granularity is 8 mV, which results in that many noise curves could not be resolved properly. The threshold DAC on the insert was connected therefore to a board DAC increasing the granularity to 2 mV.

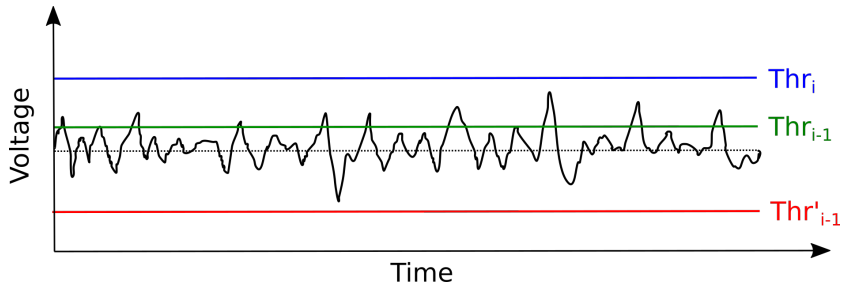

Figure 55: Possible impact of a too high threshold step size on the noise measurment. Coming from a threshold Thr_i, a small step size to Thr_{i-1} has to be used for proper noise curve measurments. With a too big step size to Thr'_{i-1}, no noise curve can be measured.

8.4 Noise Tuning of a sensor subdivision

In view of the readout limitations described in Section 8.1, the noise tuning was tested on a subdivision of the sensor matrix. For reasons of comparability, the same quadrant of 64 × 50 pix as in Section 7.3 was used. In order to determine Thr_{noise}, the lowest threshold value showing a noise rate above $f_{max} = 5\,\text{Hz}$ was chosen. An example of a measured noise curve can be seen in Figure 56a. The measured distribution of Thr_{noise} across the tuning subdivision is given in Figure 56b. Since during the investigation of the signal tuning the TDAC influence on

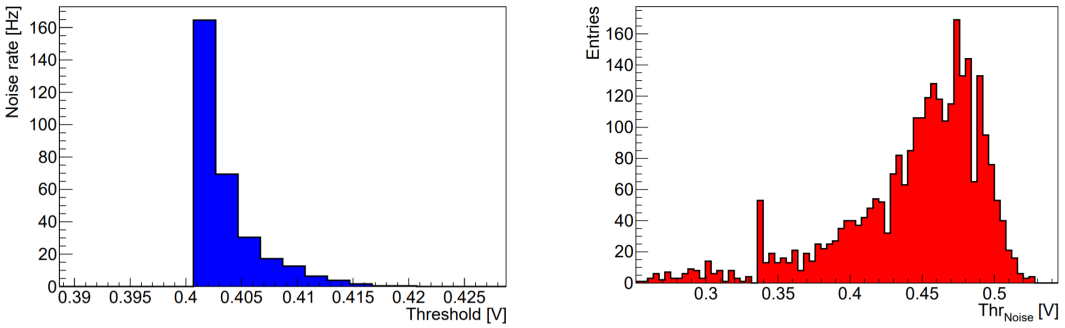

(a) Example of a measured noise curve.

(b) Measured untuned Thr_{noise} distribution.

Figure 56: Measurement of Thr_{noise}.

the threshold was found to be linear, the effect on Thr_{noise} is also assumed to have this property. Therefore, the method of calculating the TDAC value for each pixel can be simplified. This simplification consists in dividing the untuned Thr_{noise} distribution into 8 equal parts. Every part is then assigned to one TDAC value based on its difference to the target threshold. Afterwards, every pixel within a part is assigned to the corresponding TDAC value. An illustration of this is given in Figure 57a. Regarding the resulting TDAC distribution 57b, one sees that the distribution from a TDAC value of 1 to a TDAC value of 7 follows a Gaussian

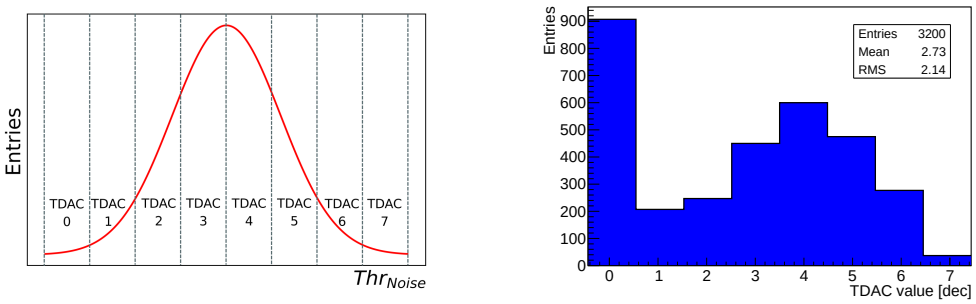

(a) Illustration of the simplified tuning method.

(b) Measured untuned Thr_{noise} distribution.

Figure 57: Determination of the TDAC set for the noise tuning.

shape. However, the peak at a TDAC value of 0 results from the large tail of the untuned Thr_{noise} distribution. From this distribution, a target threshold of 390 mV was chosen. Then, the necessary VPDAC value was estimated manually. It was chosen by setting all TDAC values to 7, setting the global threshold to the target threshold, and then varying VPDAC until some noise was observed. This guarantees a sufficient tuning range for the pixels with the highest distance to the target threshold. In this measurement, the VPDAC value was chosen to be 7. The overall tuning result is depicted in Figure 58. However, the measurement shows multiple problems. First, the initial distribution does not follow a Gaussian shape as theoretically expected. Second, the measured values of Thr_{noise} are all below the expected baseline of 475 mV. Also the tuned distribution shows problems. Here, a maximum around the desired target threshold value 390 mV was observed, but the integral of the measured part of the distribution does not match the integral of the untuned distribution. For those reasons the noise tuning could not be completed in the scope of this thesis. A discussion of the results is given in Section 9.2.

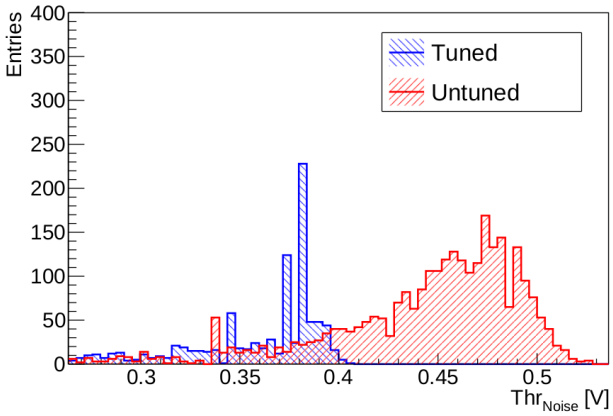

Figure 58: Comparision of the untuned and the tuned Thr_{Noise} distribution.

Part V

Discussion

9 Discussion of the tuning results

9.1 Signal tuning

First, the signal tuning was carried out on a subdivision of 3200 pix of the sensor matrix. Here, it was verified that the TDAC dependency of the threshold is linear and its slope is with a spread of 12.5 % uniform as designwise intended. Furthermore, it was shown that with a VPDAC value of 0xA the mean of the pixel threshold distribution can be shifted around 80 mV, which is sufficient for the sensor tuning. This is a huge improvement compared to MuPix8, where, while tuning was possible in principle, its impact with settings for high efficiency and good time resolution was too weak in order to uniform the sensors response [18]. With the signal tuning, a significant reduction of the pixel threshold spread from 11 mV to 4.8 mV was achieved. This result shows a high potential in terms of signal uniformity improvement on MuPix10.
However, this result has also to be taken with a grain of salt. In the first place the tuning was performed using an imperfect DAC configuration since no optimized configuration was not available by the time of the measurements. The used DAC configuration is given in Appendix B.2 in the Appendix. Also, the used setup showed a significantly higher power consumption as intended due to a configuration problem on the insert PCB found during the analysis of this thesis. This also could have lead to additional systematic errors. Additionally, in order to measure an adequate injection area, an injection voltage of 1.8 V was used. As investigated later on, this voltage is off the working point of the amplifier and therefore leads to a signal saturation. Another systematic influence which was observed is the choice of injection area, whose size and shape were found to have significant impact on the signal amplitude. Furthermore, for the full sensor tuning a spatial dependence of the pixel threshold was observed. This pattern highly affects the choice of TDACs on the sensor and could possibly add systematic effects to the sensor if its introduced artificially e.g. by the injection.

9.2 Noise tuning

As a second method, noise tuning was investigated on the same subdivision of 3200 pixels. Here, it was verified that the application of tuning is capable of decreasing the distribution of Thr_{noise} significantly. Nonetheless, the measured distributions did not match the theoretical expectation. First, the initial, untuned distribution was expected to follow a Gaussian shape. However, the measured one showed a long tail going to lower thresholds. A possible reason for this could be

non-linear behaviour of the threshold at low values. This would lead to a wrong association of the hit information to the linear assumed threshold and therefore might artificially create a tail at the lower part of the distribution. Another reason for it could again be the unoptimized DAC configuration which was used for the measurements. This configuration might have lead to a setting of the comparator off the desired working point. Furthermore, the major part of the distributions seems to be at thresholds below the baseline. Unfortunately, the baseline could not be directly measured on the used sensor. Here, it was just estimated to 475 mV using similar working DACs on another sensor. Since the baseline is also off the per design intended value of 500 mV, this could have also affected the cells working point. A further investigation on this was not possible in the scope of this thesis. Also, the measurement procedure of the noise itself showed many issues. Due to the implementation of the successive pixel masking, the TDAC sequence had to be loaded into the sensor every time pixels exceeded the maximum noise rate. Since here no option for adjusting the bit sequence only for one pixel was implemented, the whole sensor matrix had to be reconfigured with each masking procedure. Unfortunately, due to a yet unresolved software problem on FPGA side, many reconfigurations of the sensor lead to a crash of the data acquisition PC. Therefore, the system had to be restarted often during a scan which might have lead to discontinuities within the measured distributions.

10 Comparison of the tuning methods

Within this section, the three investigated tuning methods are compared and a possible utilization within the context of the Mu3e experiment is shortly discussed. To begin with the signal tuning, its goal is to achieve a uniform signal response across the sensor matrix. For its procedure, an external source of signal is required. In this thesis, test pulse injection was chosen since it provides clear and adjustable signals. However, due to the observed limitation of the injection area, the tuning was carried out part-by-part. Therefore, even with the use of high rates, a full sensor tuning using injection needs significantly more time than tuning the sensor at once. For a possible large scale implementation for the whole detector, this is a clear disadvantage. Additionally, an injection tuning in subdivisions might add systematic errors into the detector. Nevertheless, if the method should be applied to Mu3e, the injection limitations have to be investigated further and if the circumstances require, it has to be adjusted with the next phase of chip design, i.e., MuPix11.
The method of noise tuning aims for a uniform noise response of the detector. As a result of the tuning, the detection efficiency is expected to improve since it ensures that all pixels can operate at the minimum possible threshold. The main advantage of the noise tuning compared to the signal tuning is its independence on external signals like injection or radioactive sources. Since noise is an intrinsic feature of the pixel, noise tuning reduces the amount of possible systematic errors. However, the high rates which need to be processed within the noise tuning can lead to saturation in the readout system. Nevertheless, with a fast online implementation of the noise tuning on the FPGA, the limitation could be avoided.
If noise and signal are amplified equally, a uniformity of signal response would directly lead to a uniformity in noise. Therefore, the signal tuning would also lead to an improvement of the detection efficiency since lower thresholds can be applied. However, if the methods are found to be not equivalent, the signal tuning would loose operational importance.
The third method discussed in this thesis is the timing tuning. With it, the latency distribution of the pixel matrix can be narrowed which is assumed to improve the immediate time resolution of the detector. However, as already discussed in Section 5.3.3, a proper timing tuning of MuPix10 is expected to require a threshold increase in the order of 40 mV and therefore might affect the sensor's efficiency. Since efficiency weighs more for the MuPix sensors than an improvement in timing, the tuning is not of high operational interest.
In conclusion, one can say that from an operational point of view, signal and noise tuning are the methods which are most suitable for the MuPix sensors since they

are expected to equivalently increase the detector's efficiency. However, using signal tuning might add systematic effects to the calibration method and requires an optimization of the injection distribution for MuPix11. In comparison, noise tuning comes with a limitation on the readout. Nevertheless, if the tuning is directly implemented on the FPGA and verified to work, it is operationally the better choice.

11 Summary and Outlook

Within this thesis, three tuning methods for pixel sensors have been discussed: signal tuning, noise tuning and timing tuning. The method of signal tuning was first implemented and tested on a sensor subdivision of 3200 pixels. Here, the pixel threshold spread was significantly reduced from a value of 14 mV to a value of 4.7 mV. With the implementation of a part-by-part tuning using a even smaller simultaneous injection area, the spread was reduced from a value of 11 mV to a value of 4.8 mV. However, the implementation of signal tuning for the Mu3e detector would require a further investigation of the injection distribution and a resulting design adjustment. This can be considered for the next sensor generation, i.e., MuPix11.
Additionally to the signal tuning, the method of noise tuning was investigated on the same subdivision. Here, yet unresolved effects lead to a noise distribution that did not match the expectation. As a result, the tuning did not work as intended. However, it was shown that the distribution can be shifted towards lower thresholds, which in general indicates a working tuning mechanism. Here, a further investigation with an optimized DAC configuration should be carried out. To overcome the observed readout bottle necks of the measurements, a faster method directly on FPGA should be implemented.
In order to investigate the operational relevance of the signal tuning method, a study on the possible equivalence of noise and signal amplification has to be carried out. Based on this and the possible noise tuning result, a final decision on the pixel tuning method for Mu3e can be taken.

Part VI

Appendix

A Additional Plots

A.1 Power consumption of VPDAC

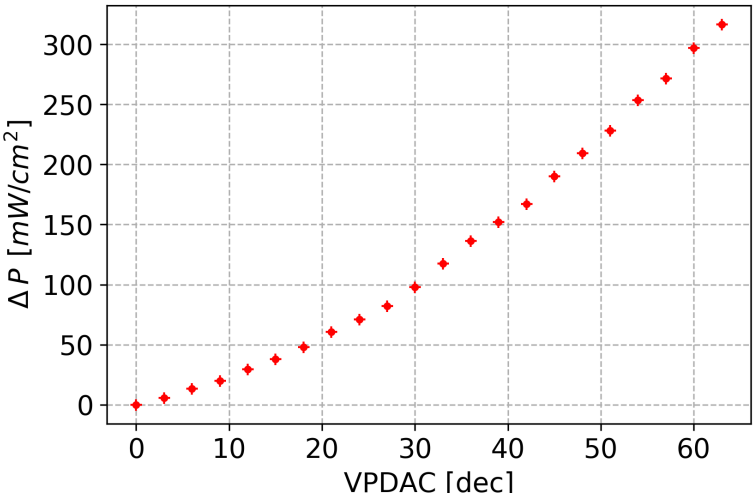

Figure 59: Relative increase of the power consumption as function of VPDAC. Every measured value was corrected for the initial power consumption at VPDAC=0.

A.2 TDAC influence on the pixel threshold

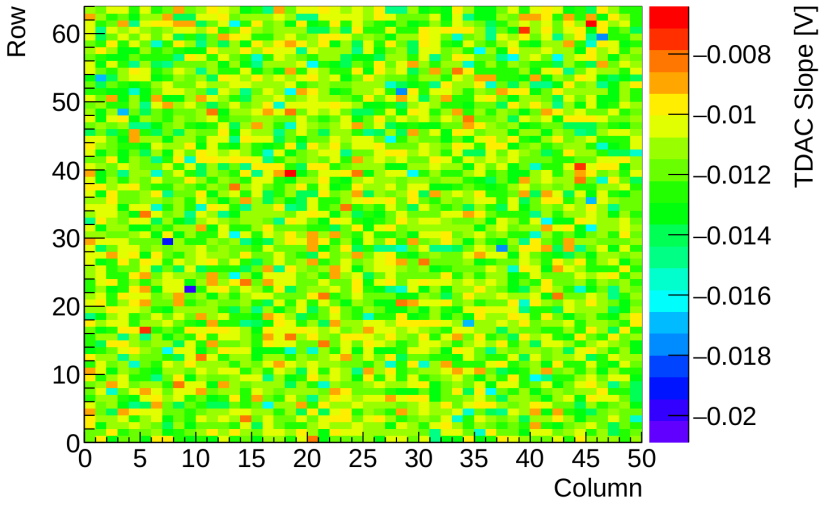

Figure 60: Distribution of TDAC slopes across the sensor subdivision. Here, no spatial correlation is visible.

A.3 Pixel threshold map for the sensor subdivision

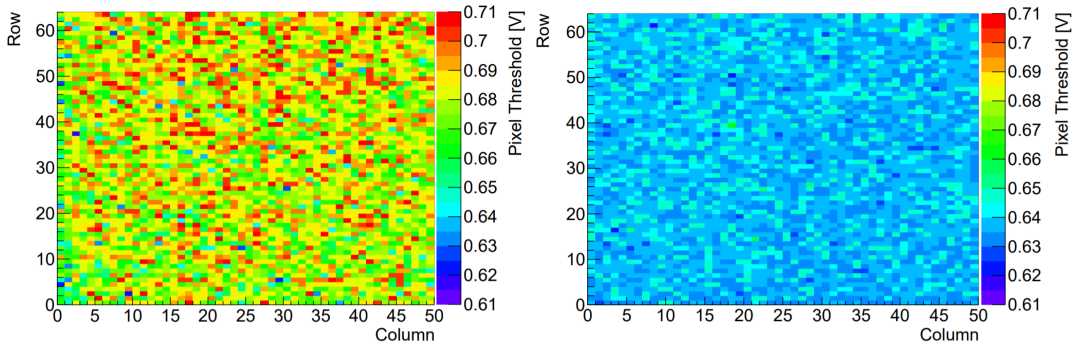

(a) Untuned pixel threshold map.

(b) Tuned pixel threshold map.

Figure 61: Comparision between the untuned and tuned pixel threshold distribution across the tuning subdivision.

A.4 Sigma distribution

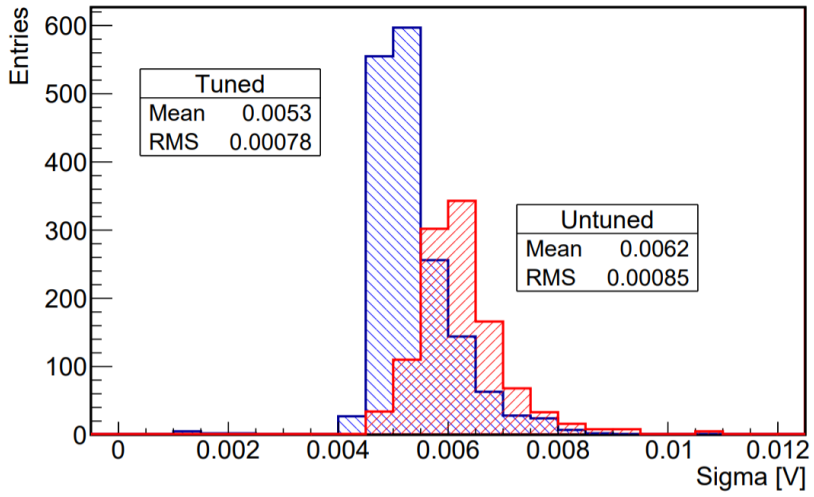

Figure 62: Comparison of the sigma distribution of the fitted s-curves for the untuned and signal tuned sensor subdivision.

B Experimental settings

B.1 Injection settings

Variable	Setting
Injection voltage	1.8 V
Pulse duration	40 ms
Frequency	100 Hz
Number of injections	5000

Table 1: Used injection settings for the signal tuning.

B.2 DAC configuration

DAC	Setting [hex]
BLResPix	5
VNPix	c
VNFBPix	14
VNPix2	0
VNBiasPix	0
VPLoadPix	5
VNOutPix	f
VNDel	a
VPComp1	0/d (signal/noise tuning)
BLResDig	5
VPComp2	d
VPTimerDel	3
VPComp2	d
Baseline	37
BLPix	6e

Table 2: Used DAC configuration. Here, only DAC values wich change the performance of the analogue or digital cell are listed.

C Bibliography

[1] *Standard Model of Elemtary Particles*. WIKIMEDIA COMMONS. URL: https://upload.wikimedia.org/wikipedia/commons/0/00/Standard_Model_of_Elementary_Particles.svg. accessed on the 06/28/2020.

[2] M. Tanabashi et al. "Review of Particle Physics". In: *Phys. Rev.* 98 (Aug. 2018), p. 030001. DOI: 10.1103/PhysRevD.98.030001.

[3] G. López Castro G. Hernández-Tomé and P.Roig. "Flavor violating leptonic decays of τ and μ leptons in the Standard Model with massive neutrinos". In: *ArXiv e-prints* (2018), pp. 18, 19. DOI: 10.1140/epjc/s10052-019-6563-4.

[4] A. Blondel et al. "Research Proposal for an Experiment to Search for the Decay $\mu \to eee$". In: *ArXiv e-prints* (Jan. 2013), pp. 15, 21, 22. arXiv: 1301.6113.

[5] U. Bellgardt et al. "Search for the decay $\mu^+ \to e^+e^+e^-$". In: *Nucl. Phys.* B299.1 (1988). DOI: 10.1016/0550-3213(88)90462-2.

[6] W. J. Marciano T. Mori and J. M. Roney. "Charged Lepton Flavor Violation Experiments". In: *Ann.Rev.Nucl.Part.Sci.* 58 (2008), pp. 315–341. DOI: 10.1146/annurev.nucl.58.110707.171126.

[7] K. Arndt et al. *Technical design of the phase I Mu3e experiment*. Tech. rep. Mu3e Collabration, Sept. 2020. arXiv: 2009.11690.

[8] H. Augustin. "Characterization of a novel HV-MAPS Sensor with two Amplification Stages and first examination of thinned MuPix Sensors". MA thesis. Heidelberg University, 2014.

[9] S. M. Seltzer and M. J. Berger. "Improved Procedure for Calculating the Collision Stopping Power of Elements and Compounds for Electrons and Positrons". In: *International Journal of Applied Radiation and Isotopes* 35 (1984), p. 27. DOI: https://doi.org/10.1016/0020-708X(84)90113-3.

[10] *Pn-junction*. WIKIMEDIA COMMONS. URL: https://commons.wikimedia.org/wiki/File:Pn-junction-equilibrium-graphs.png. accessed on the 07/08/2020.

[11] U. Husemann. *A New Pixel Detetcor for the CMS Experiment*. URL: http://ekpwww.etp.kit.edu/~husemann/talks/husemann_cms_pixel_heidelberg_20120508.pdf. accessed on the 07/09/2020.

[12] I. Peric A. Weber H. Augustin. *MuPix 10 Documentation*. Mu3e Internal Notes. Sept. 2020.

[13] *Readout concept of the MuPix sensors*. Mu3e Internal Notes.

[14] *Stratix IV GX FPGA Development Board Reference Manual*. Altera Corporation. San Jose, CA, United States, 2012.

[15] L. Huth. “A High Rate Testbeam Data Acquisition System and Characterization of High Voltage Monolithic Active Pixel Sensors”. PhD thesis. University of Heidelberg, 2018.

[16] J. Hammerich. “Analog Characterization and Time Resolution of a large scale HV-MAPS Prototype”. MA thesis. Heidelberg University, 2018.

[17] David Immig. Private communication.

[18] Heiko Augustin. Private communication.

Acknowledgements

First of all, I want to thank Prof. Dr. André Schöning for giving me the opportunity to work at a cutting edge particle physics experiment and for entrusting me with such an interesting and challenging project.

My sincerest thanks also to my second examiner Prof. Dr. Silvia Masciocchi for reading this thesis.

Furthermore, I want to thank Dr. Luigi Vigani, who always dedicated lots of his time supporting me with my project and keeping me motivated with his endless passion.

I also want to thank Heiko Augustin, who helped me sorting my thoughts in times of confusion and gave me and this thesis a thread.

Additionally, I would like to thank David Immig who taught me C++ during the COVID-19 lockdown and therefore helped me to make use of this special time.

Also, thanks to my parents for their love and support during the time of my Bachelor.

Finally, I want to thank the rest of the Mu3e and ATLAS group for helping me with various issues and for making my time here such a great experience.

Erklärung

Ich versichere, dass ich diese Arbeit selbstständig verfasst und keine anderen als die angegebenen Quellen und Hilfsmittel benutzt habe.

Heidelberg, den 16.10.2020,